



AMERICAN METEOROLOGICAL SOCIETY

Journal of Physical Oceanography

EARLY ONLINE RELEASE

This is a preliminary PDF of the author-produced manuscript that has been peer-reviewed and accepted for publication. Since it is being posted so soon after acceptance, it has not yet been copyedited, formatted, or processed by AMS Publications. This preliminary version of the manuscript may be downloaded, distributed, and cited, but please be aware that there will be visual differences and possibly some content differences between this version and the final published version.

The DOI for this manuscript is doi: 10.1175/JPO-D-12-067.1

The final published version of this manuscript will replace the preliminary version at the above DOI once it is available.

If you would like to cite this EOR in a separate work, please use the following full citation:

Elipot, S., C. Hughes, S. Olhede, and J. Toole, 2013: Coherence of western boundary pressure at the RAPID WAVE array: boundary wave adjustments or deep western boundary current advection?. *J. Phys. Oceanogr.* doi:10.1175/JPO-D-12-067.1, in press.



1 **Coherence of western boundary pressure at the RAPID WAVE**

2 **array: boundary wave adjustments or deep western boundary**

3 **current advection?**

4 **SHANE ELIPOT *AND CHRIS HUGHES**

National Oceanography Centre, U.K.

5 **SOFIA OLHEDE,**

University College London, London, U.K.

6 **JOHN TOOLE**

Woods Hole Oceanographic Institution, Woods Hole, MA, U.S.A

* *Corresponding author address:* Shane Elipot, National Oceanographic Centre, Joseph Proudman Building, 6 Brownlow Street, Liverpool, L35DA, UK.

E-mail: shane.elipot@noc.ac.uk

ABSTRACT

We investigate the coherence between ocean bottom pressure signals at the the RAPID WAVE array on the western North Atlantic continental slope, including the Woods Hole Oceanographic Institution Line W. Highly coherent pressure signals propagate southwestward along the slope, at speeds in excess of 128 m s^{-1} , consistent with expectations of barotropic Kelvin-like waves. We also see coherent signals in the smaller pressure differences relative to 1000 m depth, which are expected to be associated with depth-dependent basin-wide meridional transport variations, or an overturning circulation. These signals are coherent and almost in phase for all time scales from 3.6 years down to 3 months. Coherence is still seen at shorter time scales for which group delay estimates are consistent with a propagation speed of about 1 m s^{-1} over 990 km of continental slope, but with large error bounds on the speed. This is roughly consistent with expectations for propagation of coastally-trapped waves, though somewhat slower than expected. A comparison with both Eulerian currents and Lagrangian float measurements shows that the coherence is inconsistent with a propagation of signals by advection, except possibly on time scales longer than 6 months.

1. Introduction

Under a changing climate, it is of crucial importance to identify the processes by which adjustments of the Atlantic Meridional Overturning Circulation (MOC) take place in the real ocean. As atmospheric forcings vary, MOC anomalies at high latitudes triggered by changes in deep water formation travel equatorward along the western boundary as coastally-trapped

28 waves, leaving in their wake altered circulations and meridional transports (Johnson and
29 Marshall 2002). Eventually, anomalies should also be distributed by advective means, either
30 by the Deep Western Boundary Current (DWBC) or via interior routes, as partly evidenced
31 by numerical simulations (Zhang 2010), Lagrangian observations (Bower et al. 2009), or water
32 mass diagnostics (Peña-Molino et al. 2011). Simultaneous observations of MOC variability
33 as a function of time and latitude are lacking to verify these theoretical expectations, derived
34 for idealized or approximated oceanic configurations. Furthermore, the real ocean presents
35 intricate topography, continuous stratification, and horizontal circulations which complicate
36 this simple picture.

37 This paper investigates the relationships between observations of pressure at three moor-
38 ing lines on the continental slope of the western North Atlantic (Fig. 1), part of the RAPID
39 West Atlantic Variability Experiment (WAVE). The underlying motivations for these obser-
40 vations are that boundary pressures are in theory proportional to zonally integrated merid-
41 ional transports, while boundary pressure gradients are proportional to the vertical shear,
42 or overturning component of those transports (Hughes et al. 2012). Bingham and Hughes
43 (2008) showed in an ocean global circulation model (OGCM) how the boundary pressure
44 and directly zonally-integrated transports time series are related in a way that is consistent
45 with the zonally-integrated geostrophic zonal momentum balance. We use here observations
46 of boundary pressure time series to test the hypothesis that the western boundary commu-
47 nicates pressure anomalies. This mechanism has been put forward in numerical studies to
48 explain the meridional coherence of the MOC (Roussenov et al. 2008).

49 This paper is organized as follows. Section 2 contains a short review of the concept of
50 bottom pressure on eastern and western boundaries as a measure of zonally-integrated merid-

51 ional transport across an ocean basin, and provide the motivation for this study. The same
52 section then exposes briefly the theoretical expectations for boundary waves applicable to
53 our observations. Section 3 describes the relevant data from RAPID WAVE used to analyze
54 boundary pressures and pressure gradients. Section 4 describes the methods employed to
55 derive the pressure gradient time series at two mooring lines. Section 5 presents the results
56 of correlation, coherence and delay estimations of pressure and pressure gradient time series,
57 and compares the results to expectations. Section 6 provides a summary and concluding
58 remarks.

59 **2. Theoretical considerations and expectations**

60 *a. Meridional transport and western boundary pressure*

61 Integrating horizontally across an ocean basin section the zonal geostrophic momen-
62 tum balance $\rho f v = \partial p / \partial x$ (where ρ is the in-situ density, f the Coriolis frequency, and v
63 the meridional velocity) shows that the meridional mass transport per unit depth $M(z) =$
64 $\int_{x_W}^{x_E} \rho v dx$ is the difference between the bottom pressure at depth z on the eastern slope at
65 longitude $x_E(z)$ and the bottom pressure on the western slope at $x_W(z)$:

$$66 \quad fM(z) = -p_W(z) + p_E(z). \quad (1)$$

67 As will be seen from the data presented in Section 3, much of the pressure variability is
68 independent of depth on the slope. But an overturning circulation must by definition change
69 direction with depth and hence involves pressure anomalies which vary with depth. In order
70 to focus on the overturning component of the transport, we consider the vertical derivative

71 of (1):

$$72 \quad f \frac{\partial M(z)}{\partial z} = -\frac{\partial p_W(z)}{\partial z} + \frac{\partial p_E(z)}{\partial z}, \quad (2)$$

73 which relates the vertical shear of the mass transport $\partial M/\partial z$ to two boundary pressure
74 gradient terms; the first term $-(\partial p_W/\partial z)/f$ defines the western boundary contribution to the
75 overturning transport, and the second term $(\partial p_E/\partial z)/f$ the eastern boundary contribution.
76 See Hughes et al. (2012) for a comprehensive discussion of this formulation.

77 An immediate question is which of these two terms, which can be estimated indepen-
78 dently, is more important for variability in the zonal integral. Using 19 years of OGCM
79 data, Bingham and Hughes (2008) showed that interannual variability in volume transport
80 between 100 and 1300 m at 42°N in the Atlantic Ocean could be calculated from (1) us-
81 ing only bottom pressure from the western boundary with a skill¹ of 92%. In the deeper
82 layer between 1300 and 3000 m the skill reached 96%. Thus, the eastern boundary plays
83 very little role in interannual variability within the model. The relative importance of each
84 boundaries has been studied from observations of the 26°N RAPID MOC array by Kanzow
85 et al. (2010). They showed that the western boundary dominated the total variance (2.0 Sv
86 [1 sverdrup (Sv) = 10⁶ m³ s⁻¹] versus 1.3 Sv r.m.s. amplitude of the variations), despite
87 the control of the annual cycle by the eastern boundary (Chidichimo et al. 2010). We focus
88 here on the western boundary variability, which is expected to reflect first the propagation
89 of disturbances from high to low latitudes.

¹the skill of a variable y to represent another variable x is $1 - \sigma^2(x-y)/\sigma^2(x)$ where $\sigma^2(x)$ is the variance of x .

90 *b. Connectivity of transports*

91 At multi-annual time scales, advection of water masses at depth by the fast DWBC and by
92 the slower so-called interior pathways eventually carry density anomalies and modify zonally
93 integrated transport between boundaries (e.g. van Sebille et al. 2011). At relatively shorter
94 time scales –in a matter of months– the meridional coherence of transports is expected to
95 be achieved by the propagation of disturbances in the pressure and velocity fields carried
96 by subinertial boundary waves. All such waves propagate cyclonically around the ocean basin
97 (Huthnance 1978) and hence carry signals southward along the western boundary. Model
98 studies (Bingham et al. 2007) suggest that some signals propagate rapidly from north to
99 south, but there is a significant decoupling between subpolar and subtropical MOC variability
100 at interannual to decadal periods. We provide here a short review of the theories and present
101 some specific expectations for our region of study.

102 1) THEORIES OF BOUNDARY WAVES

103 The combination of the effects of topography, stratification and planetary vorticity pro-
104 duces a wide variety of wave modes in the ocean (Rhines 1970). At the continental slope
105 neglecting the β -effect in comparison with the steep topography, Huthnance (1978) showed
106 that this resulted in an infinite, discrete sequence of coastally-trapped waves (CTW). In the
107 extreme case of a stratified ocean with a steep sidewall spanning much less than a baroclinic
108 Rossby radius of deformation in the horizontal, these waves are a series of Kelvin waves as
109 found in the study of Johnson and Marshall (2002). The other extreme, of sloping topog-
110 raphy and no stratification, leads to topographic Rossby waves (TRW) (Wang and Mooers

111 1976). In all cases in the northern hemisphere, the phase of these waves propagates with
112 the shallow topography to their right, and in the long wave limit the group velocity is in the
113 same direction. These are therefore the wave modes which we would expect to communicate
114 pressure changes resulting from high latitude processes to lower latitudes, along the western
115 boundary.

116 2) O’ROURKE (2009)’S CALCULATIONS FOR REALISTIC CONDITIONS

117 For our purpose, we will consider and report here some relevant results from the wave
118 study of O’Rourke (2009) who specifically examined the possible characteristics of Kelvin-like
119 waves and CTW on the western boundary of the North Atlantic, for long wavelength waves
120 (i.e. in the limit of frequency $\ll f$, appropriate for most of the signals we are considering
121 here). She calculated the structure of the pressure field of waves and their along slope speeds
122 at a number of discrete topographic profiles extracted from the GEBCO dataset (IOC, IHO,
123 and BODC, 2003) between 28°N and 43°N. She solved numerically the continental shelf
124 wave vorticity equation for the free surface barotropic cases, and she used the BIGLOAD2
125 program of Brink and Chapman (1985) for the baroclinic cases, with an offshore density
126 profile calculated from the temperature-salinity climatology of Lozier et al. (1995).

127 O’Rourke (2009)’s study produced propagation speeds for the gravest mode for the
128 barotropic case in the range 170–220 m s⁻¹ for the region. This wave mode 0 is effec-
129 tively a deep-ocean barotropic Kelvin wave mode (Wright and Xu 2004), and would not be
130 greatly affected by the presence of stratification, as in the real ocean. The natural length
131 scale for these waves, perpendicular to isobaths, is the barotropic Rossby radius (\sqrt{gH}/f),

132 which is about 2000 km here. These wave modes have very little structure over the width
133 of the continental slope, and therefore should produce a western boundary pressure signal
134 which is almost independent of bathymetry and depth.

135 For the higher modes including stratification, because of the complexity of the real to-
136 pography, the BIGLOAD2 program did not return a consistent picture of CTW modes at
137 different positions along the boundary between 28°N and 43°N. Nonetheless, we present
138 as an example her results for a carefully examined topographic section centered at 40.5°N
139 which is highlighted in Fig. 1. This section is typical of the wide shelf configuration found in
140 our study region, and should provide a useful point of comparison for the delays estimated
141 between the transport time series based on pressure gradients derived in section 4. The
142 pressure structure of the first 3 baroclinic wave modes and their associated wave speeds are
143 shown in Fig. 2. Mode 1 with one zero crossing of the pressure along the slope is not a pure
144 coastal baroclinic Kelvin wave but a wave modified by the sloping topography and stratifi-
145 cation, with isolines of pressures tilted over a horizontal lengthscale comparable to the slope
146 itself. With a first baroclinic Rossby radius Ro in this region of about 20 km (Chelton et al.
147 1998), the expected scaling for the tilt of nodal lines of $NH/fL = 1$ leads to a horizontal
148 displacement of the nodal line between bottom and top of the ocean of about $\pi Ro \approx 60$ km,
149 which is a good match for the displacements we see. The speed of this wave at this section
150 is 5.13 m s^{-1} , which is approximately a lower limit for all other speeds that O'Rourke (2009)
151 diagnosed between 28°N and 43°N for this mode. This first baroclinic mode is somewhat
152 faster than the $O(1) \text{ m s}^{-1}$ value usually found for the baroclinic Kelvin wave seen in an
153 idealized two-layer vertical sidewall basin (Johnson and Marshall 2002). Modes 2 and 3,
154 with respectively two and three zero crossings in bottom pressure, have more complicated

155 structures for the pressure field along the slope than for the wave mode 1. These do not have
156 the vertical nodal contours of barotropic mode, or the horizontal nodes of pure baroclinic
157 Kelvin waves, but are truly hybrid modes, showing a degree of bottom trapping (Huthnance
158 1978). They have here relatively slower wave speeds at 3.30 m s^{-1} for mode 2 and 1.47 m
159 s^{-1} for mode 3.

160 **3. Data**

161 *a. RAPID WAVE deployment and recovery cruises*

162 Investigators of the UK National Oceanography Centre (NOC) deployed an observational
163 array called RAPID WAVE since April 2004 (Fig. 1) as part of the wider UK RAPID
164 Climate Change programme. The WAVE array originally consisted of three measurement
165 lines spanning the continental slope: lines A and B were instrumented by NOC, which also
166 supplemented additional instruments along WHOI Line W (Toole et al. 2011) (Fig. 3). Lines
167 A and B originally included six lander Bottom Pressure Recorders (BPR) each, which were
168 deployed during the *RSS Charles Darwin* cruise 160 in Aug. 2004. During the *RSS Discovery*
169 cruise 308 in Jul.–Aug. 2006 only BPRs A0, A1, B0, B1, B2, and B3 were recovered. In
170 view of the BPR losses, Line A was abandoned and six BPRs at Line B (B0 to B5) were
171 redeployed. In Oct. 2007 during the *CCGS Hudson* expedition 2007-045 the BPRs B2, B3,
172 B4 and B5 were recovered and redeployed. In Sept.–Oct. 2008 during the *CCGS Hudson*
173 expedition 2008-037 these BPRS were all recovered except B1. At that time Line B was
174 replaced by the RAPID-Scotian Line in collaboration with the Canadian Bedford Institute

175 of Oceanography (Hughes et al. 2012) but the data from this new line are not used here.

176 At Line W, the WAVE operations for 2004–2008 took place during five cruises: six BPRs
177 were deployed (W0 to W5) during the *R/V Oceanus* cruise 401 in 2004 ; only two BPRS
178 were recovered (W0, W1) and the others lost, and three were redeployed (W0, W1, W2)
179 during the *R/V Oceanus* cruise 421 in Apr. 2006 ; two of these three BPRs (W0, W1) were
180 recovered and three redeployed (W0, W1, W5) during the *R/V Oceanus* cruise 446 in May
181 2008; W4 was recovered and W3 was deployed during the *R/V Endeavor* cruise 454 in Sept.
182 2008. Eventually, the W2 BPR was recovered during the 2010 *R/V Atlantis* cruise 17 but
183 its record extended only into 2008.

184 *b. Bottom Pressure Recorder processing*

185 Only a usable subset of the quality controlled and processed 15-min interval BPR records
186 of the WAVE array are considered for this study (Fig. 4). Unfortunately, electronics problem
187 resulted in some of the earlier deployments producing sporadic false data but rarely lasting
188 more than a few hours at a time. False points were identified by comparison with an
189 average of neighboring points in time (after subtraction of tides fit to the good points, thus
190 requiring some iteration). Gaps shorter than one day were filled by a combination of linear
191 interpolation of tidal residual plus short period variability taken from a neighboring good
192 record from the same line. Spectra of the resulting time series and of differences between
193 neighboring records (not shown) revealed that pressure differences contain a factor of 100 less
194 power than the total pressure, in a band between the inertial period and about 5 days. The
195 noisy records, after replacement of bad points, generally showed similar difference spectra

196 at periods longer than about 2.5 days, suggesting that the editing procedure was acceptable
197 at these periods. Nonetheless, the records from the 2006 deployments at B0 and B2 remain
198 noticeably noisier than others. Finally, an exponential-linear trend with time (Watts and
199 Kontoyiannis 1990) was also removed from each record, typically with a range of a few tens
200 of mbar or less (in one case reaching a range of 109 mbar).

201 *c. Selected WHOI Line W velocity and density records*

202 Woods Hole Line W spans the continental slope from 38°N to 40°N, roughly perpendicular
203 to isobaths (Figs. 1 and 3). Details about deployment history and instruments can be found
204 in Toole et al. (2011). In order to derive the pressure gradient down the slope at Line W (see
205 section 4), data from near-bottom fixed instruments were used. The data from the McLane
206 Moored Profiler (MMP) on mooring W1 were also used to obtain an estimate of near-bottom
207 density and velocity at two depth levels, 1000 m and 1788 m (Fig. 3). This last depth level
208 corresponds to the depth of an additional short mooring holding a BPR, called here W0,
209 deployed originally in 2004 as part of WAVE. All the velocity and temperature-salinity near-
210 bottom instruments used returned good data with three exceptions. At mooring W1 the
211 near bottom current meter failed from 6 Dec. 2004 incurring a gap in the record until 30
212 Apr. 2005. At mooring W4, the near-bottom Acoustic Doppler Current Profiler located 111
213 m above bottom failed for the 2004-2006 deployment so that an estimate of the near-bottom
214 velocity was taken from the Vector Averaging Current Meter (VACM) 452 m above the
215 bottom instead. The MMP on W1 failed between mid-April 2006 and early April 2007, and
216 synthesized data for this time period were created similarly to Toole et al. (2011), based on

217 regressions between the data from MMPs at this site for the other time periods, and the data
218 of the fixed sensors at the top and bottom of W1. The high-sampling-rate fixed instrument
219 data records were lowpass filtered to retain frequencies less than 1 cycle per day (cpd) then
220 sampled every 12-h. The MMP at W1 was programmed to burst sample every 5th day a set
221 of 4 one-way profiles, which are averaged here to reduce inertial and tidal oscillations. The
222 5-day interval times series were then interpolated linearly every 12-h for consistency with
223 the other time series. The resulting near-bottom velocity and density records are shown in
224 Fig. 5. Note that the data from the rest of the Line W instruments are also used here to
225 derive the volume transport within the trapezoidal region formed by the array (see section
226 4).

227 4. Methods

228 In this section we explain the methods which were implemented to derive at Line W and
229 at Line B the western boundary pressure gradient time series and their associated integrated
230 form as western boundary transports below and relative, that is referenced, to 1000 m.

231 *a. Calculating pressure differences at Line W*

232 One of the two methods of Hughes et al. (2012) is used to derive the western boundary
233 pressure gradient $\partial p_W / \partial z$ at Line W, relative to 1000 m. The methods allow to reconstruct
234 boundary pressure gradients from near-bottom measurements of density and velocity along
235 a continental slope. The result is a drift-free estimate of pressure gradient, which could not

236 be obtained otherwise by multiple deployments of BPRs at large depths, due to instrumental
 237 drift (Watts and Kontoyiannis 1990). First, as in Hughes et al. (2012), the applicability of
 238 the method chosen at Line W is tested at intra-annual time scales.

239 The method we use is a generalization of the hydrostatic equation along a sloping bottom
 240 assuming that the flow is steered by topography. The three-dimensional oceanic pressure
 241 gradient is $\nabla p = -\mathbf{k} \times (\rho f \mathbf{u}_g) - \mathbf{k} \rho g$, with \mathbf{u}_g the geostrophic velocity, g the acceleration of
 242 gravity and \mathbf{k} the upward vertical unit vector. With the z -axis positive upwards, the vertical
 243 component of the differential of the bottom pressure on the sea floor defined by $z = -H$,
 244 along a three-dimensional path of horizontal component $ds = -dz/H_s$ where $H_s = \partial H / \partial s$,
 245 is

$$246 \quad \delta p_b = - \left(\frac{\rho f u_L}{H_s} + \rho g \right) \delta z, \quad (3)$$

247 where u_L is the horizontal geostrophic velocity to the left of the horizontal component of the
 248 path (traversed in the direction from shallow toward deep water so that δz is negative). In
 249 order to test the method, first the left hand side of (3) is computed from 22 months (April
 250 2006 to February 2008) of detided and detrended pressure records from BPRs deployed at
 251 the bases of moorings W1 (2242 m depth, two deployments over this period) and W2 (2752
 252 m depth, one deployment), which are separated horizontally by 48.2 km and vertically by
 253 510 m (Fig. 3). Second, the right hand side of (3) is computed with averages of velocity and
 254 density anomalies from instruments located 116 m above the bottom at W1 and 75 m above
 255 bottom at W2.

256 Cross-spectral analysis (see the Appendix for the method employed) between the two
 257 time series (Figs. 6b and d) shows that for periods between about 7 and 90 days, the

258 pressure reconstruction explains typically more than 50% of the variance, reaching 92% in
259 some frequency bands, and is approximately in phase with the pressure difference from BPRs.
260 The coherence squared decreases dramatically for periods shorter than 7 days, as it is possible
261 that ageostrophic motions start to dominate at these time scales. The coherence squared
262 becomes not significant at periods longer than 90 days, and this is likely ascribable to the
263 detrending of the BPR records affecting their spectra more severely toward low frequencies
264 (for reference, a relatively large linear trend of 76 mbar or 7600 Pa over this nearly 2-year
265 period has been subtracted from the W2 record). In order to quantify the quality of the
266 reconstruction we therefore bandpass filter the time series to retain frequencies between 1/90
267 and 1/7 cpd, as shown in Fig. 6a. The regression coefficient of the reconstruction onto the
268 BPR pressure difference is 0.74 (scatter plot in Fig. 6c), and therefore the amount of the total
269 variance explained by the reconstruction is only 57%. The rms difference is 0.97 mbar, which
270 translates to a volume transport error of 1.05 Sv per km of depth (according to (2) with
271 $f = 0.92 \times 10^{-4} \text{ s}^{-1}$ and a reference density of 1000 kg m^{-3}) (Hughes et al. 2012). This error,
272 if sustained over 3120 m of depth, gives an error estimate for the transport of 3.2 Sv. This
273 error is comparable with the expected natural variability of transports (Cunningham et al.
274 2007), and significantly larger than the error obtained using the more favorable geometry of
275 the RAPID-Scotian Line (Hughes et al. 2012). Nonetheless, we will see that the correlation
276 between the two pressure-derived time series obtained for this study (see section 5) is an
277 a posteriori validation of their usefulness for studying the propagation of signals along the
278 boundary.

279 For the purpose of estimating $\partial p_W / \partial z$, the right hand side of (3) is applied in six discrete
280 steps from 1000 m to 4120 m down the continental slope at 12-h time interval from 11 May

281 2004 to 8 April 2008. Following the methodology of Hughes et al. (2012), the values used for
282 ρ in (3) are the in-situ density anomalies with respect to the mean density profile as we are
283 not interested in the mean hydrostatic pressure here. Other referencings of pressure could
284 be used but this only affects the mean values, irrelevant for our subsequent analyses which
285 are based on temporal anomalies. A mean pressure at each step also arises from the mean
286 velocity but once again it is not relevant for our analysis and is ignored here. In contrast to
287 the test above, the time series of reconstructed pressure differences were only lowpass filtered
288 below 1 cpd, therefore retaining variability on long time scales, including inter-annual, which
289 would not be accessible otherwise from BPR data. The first two steps, from 1000 m to W0
290 (1788 m), and then to the base of mooring W1 were computed by approximating the velocity
291 and density at these depths along the slope by the data collected by the MMP on mooring
292 W1, actually located offshore of the slope (the horizontal distance at 1000 m depth between
293 W1 and the slope is 32 km, see Fig. 3). When the near-bottom velocity record was missing
294 at W1, the velocity there was taken equal to the velocity from the MMP at the depth of W0
295 for the W0–W1 step, and equal to the velocity from W2 for the W1–W2 step.

296 The three gaps occurring in the pressure time series (maximum length 15.5 days) because
297 of mooring turnovers were filled by replacing values (initially zero) by a lowpass filtered
298 version of the time series and iterating (less than 30 times) until the rms difference between
299 iterations was less than 0.1 Pa. The data records at W5 stop about 4 months before the
300 other records, and the pressure time series there was filled by using a linear regression model
301 based on all preceding pressure data (explaining 72% of the variance at W5). The time series
302 of pressure anomalies $-p'_W(z)$, proportional to northward transports according to (1), are

303 shown in Fig. 7a for the six depth steps.

304 *b. Vertical structure of the pressure variability on the slope*

305 We analyze the vertical structure of the boundary pressure variability. At Line W,
306 the first empirical orthogonal function (EOF) of the boundary pressure $p'_W(z)$ time series
307 (Fig. 7c), which explains 81.3% of the covariance, is a monotonic function, increasing in
308 amplitude with depth. The second EOF explaining only 11% of the variance shows a kink
309 below 3500 m with a reversal of sign. At Line B we also examine the vertical structure of the
310 pressure variability by calculating the first two EOFs for three deployment periods (2004–
311 2006, 2006–2007, 2007–2008) after lowpassing the time series to retain time scales longer than
312 one day. In order to focus on the variability of pressure differences –or pressure gradient– we
313 subtract from all records the shallowest record available before computing the EOFs. The
314 results for the first two EOFs in each case are plotted in Fig. 4. The sum of the first two
315 modes explains between 92% and 99% of the variance. Similar structures to Line W are
316 found: the first EOFs are single-signed increasing with depth while the second EOFs exhibit
317 sharp reversals of sign below 3500 m. Only the second EOF for the 2004–2006 deployment is
318 very different but this one is calculated without data below 3700 m. The greater variability
319 at both lines below 3700 m approximately can be associated with bottom-trapped TRW
320 activity which has been extensively observed and described in this region (e.g. Thompson
321 and Luyten 1976; Louis et al. 1982), or we speculate to the increasing eddy activity occurring
322 over the Abyssal Plain to the south and east. Despite the bottom-intensified variability, the
323 EOF analyses at both lines suggests strongly that the part of the pressure gradient which

324 is a near linear function of depth is likely to capture a coherent mode of variability across
 325 the RAPID WAVE array. Since through the 2004–2008 period we always have at least two
 326 records available at any time shallower than 3500 m we can achieve at Line B an estimate
 327 of the boundary pressure gradient between 1000 m and 4000 m by a linear approximation
 328 as explained next.

329 *c. Calculation of transports*

330 1) LINE W

331 The pressure-derived volume transport time series anomaly T_W is computed as

$$332 \quad T_W = \int_{-4120}^{-1000} \frac{-p'_W(z)}{\rho_0 f} dz. \quad (4)$$

333 Practically a trapezoidal integration is conducted in the six discrete intervals between 1000 m
 334 and W5 at 4120 m. The resulting transport is the western boundary end-point contribution
 335 to the zonally integrated meridional transport below and relative to 1000 m depth. This
 336 time series is shown in Fig. 8 to put it in the context of the DWBC at Line W. The standard
 337 deviation of T_W is 6.5 Sv but note that the uncertainty from the pressure reconstruction is
 338 at about 3.2 Sv and thus only 24% of the signal variance. In one noticeable event lasting
 339 less than 4 days centered on 18 May 2006, T_W reached an anomaly of -37.3 Sv, associated
 340 with large anomalies of near-bottom velocity and density from W1 to W4 (Fig. 5). However
 341 this corresponds to the period when the MMP at W1 had failed and for which the data at
 342 W0 and 1000 m were estimated from the fixed instruments on W1: as such this event may
 343 be overestimated due to errors in the procedure used to fill missing data.

344 2) LINE B

345 The longest overlapping time period of single BPR deployments at Line B is 708 days
 346 (Fig. 4), a time scale which should therefore be seen as an upper limit of reliable time scales in
 347 these records. At each time step, a least-squares fit to $p_W(t, z) = a(t) + b(t)z$ was conducted
 348 to give a time series of $b(t) = \partial p_W / \partial z$. In order to account for apparent increased noise in
 349 two records from the 2006 deployment, B2 was down-weighted by a factor of 2 in the fit for
 350 this period, and B0 was down-weighted initially by a factor of 2, increasing to a factor of 3
 351 in 2007. B5 is a record clearly associated with variability below 3500 m (EOF2 in Fig. 4c)
 352 distinct from the near linear pressure gradient above (EOF1). Thus we ignored B5 in the fit
 353 to be consistent with time periods when B5 is absent. Gaps in the time series $b(t)$, between
 354 deployments, were filled by replacing values in the gaps (initially zero) by a lowpass filtered
 355 version of the time series (periods > 5 days), and iterating six times.

356 The time series $b(t)$ filtered to retain periods longer than one day is shown in Fig. 9. It is a
 357 pressure gradient time series in units of pressure per unit depth (left axis), and also converted
 358 to a pressure-derived volume transport time series T_B (right axis) between $z_1 = 1000$ m and
 359 $z_2 = 4000$ m by

$$360 \quad T_B = \int_{z_2}^{z_1} \left(\int_{z_2}^{z_1} -\frac{1}{\rho f} \frac{\partial p_W}{\partial z} dz \right) dz = \frac{b}{2f\rho_0} \Delta z^2,$$

361 with $\Delta z = z_2 - z_1 = 3000$ m, $f = 9.853 \times 10^{-5} \text{ s}^{-1}$, $\rho_0 = 1040 \text{ kg m}^{-3}$. This integration
 362 assumes that the transport per unit depth at 1000 m is a constant in time, chosen here as
 363 zero as this corresponds approximately to the zero-crossing of the MOC upper cell. Like the
 364 time series T_W derived previously T_B is a western boundary contribution to the meridional
 365 transport anomaly below and relative 1000 m depth. The effect of choosing a different

366 reference depth for T_B is to rescale the amplitudes of the variability while retaining the
367 temporal structure. The standard deviation of T_B is 5.1 Sv, which is comparable within
368 error bars to the standard deviation of T_W (6.5 Sv) which is a transport computed for the
369 same depth layer.

370 *d. Relationship between zonally-integrated and DWBC transports at Line W*

371 As an aside, it is interesting to consider the relationship between T_W and the transport
372 of the DWBC. From Line W data, Toole et al. (2011) estimated the DWBC transport
373 as the the sum of four density layer transports of Upper Labrador Sea Water, Classical
374 Labrador Sea Water, Iceland-Scotland Overflow Water, and Denmark-Strait Overflow Water.
375 Each layer transport was defined at each time step as the maximum of the streamfunction
376 computed from the westernmost mooring (W1) to the most eastern mooring (W5), in bins
377 separated horizontally by the mid-distance points between moorings. Potential biases when
378 the streamfunctions did not reach their maxima within the array were also assessed. T_W
379 is significantly anti-correlated (-0.28) with Toole et al. (2011)’s DWBC transport. Yet, we
380 find it more appropriate to compare T_W in detail to the transport within the fixed “wedge”
381 region below 1000 m formed by the continental slope to the west and W5 mooring to the
382 east, thereafter called T_{WEDGE} , plotted in Fig. 8b. T_{WEDGE} is evidently correlated (at 0.85)
383 with the DWBC transport as calculated in density layers by Toole et al. (2011).

384 T_W was lowpass filtered below 10 days and subsampled every 5 days for comparison
385 to T_{WEDGE} . The zero-lag correlation between these two time series is then -0.14, which
386 is statistically significant only at the 94% confidence level following the methodology of

387 Ebisuzaki (1997) for serially correlated time series. The clear result is that the DWBC
 388 shows much more variability than the zonally-integrated measure T_W and is only weakly,
 389 negatively, correlated with it. Given that both measures involve the current measurements,
 390 a degree of correlation is to be expected. The fact that it is a negative correlation, though
 391 surprising, is also to be expected. Combining (2) and (3) along a sloping western boundary
 392 gives:

$$393 \quad f \frac{\partial M_W}{\partial z} = -\frac{\partial p_W}{\partial z} = g\rho_W + \left(\frac{\rho f v}{\partial H / \partial x} \right)_W. \quad (5)$$

394 In the Northern Hemisphere at the western boundary where $\partial H / \partial x > 0$, at constant density,
 395 (5) predicts that the transport shear is of the same sign as the near-bottom meridional
 396 geostrophic velocity. A northward velocity will induce a positive shear in the transport so
 397 that the zonally integrated flow becomes more southward with increasing depth along the
 398 slope, which is counter-intuitive.

399 As an illustration of how this can come about, consider the illustration shown in Fig. 10
 400 which is similar to synoptic observations of across-line velocity at Line W based on ship
 401 surveys (Fig. 2 in Toole et al. (2011)) (but rather different from the Eulerian mean velocity
 402 observed by the array, Fig. 3 in Toole et al. (2011)). A barotropic (in the sense uniform in
 403 the vertical) boundary current is flowing southward over a western boundary with a velocity
 404 anomaly $-c < 0$, while to the east a barotropic current of opposite sign flows over flat
 405 topography with longitudinal extent δ . To put this situation in the context of the North
 406 Atlantic MOC we require that the net area-integrated meridional transport to be zero but
 407 this is not necessary for our purpose, only that no changes occur to the shear because of
 408 the region to the east. Setting the uniform velocity to the east to $c/(2\delta)$ can achieve both

409 conditions. The resulting volume transport anomaly per unit depth $Q(z)$ varies linearly
410 with depth, from $-c/2$ at the surface to $c/2$ at the bottom. This illustrate how a southward
411 velocity anomaly of a barotropic DWBC leads to a northward anomaly of the integrated
412 transport below a reference depth because of the changing width of the basin.

413 Directly measured transport of the DWBC on one hand, either in depth space, or in
414 density space such as in Toole et al. (2011), and a integral quantity like T_W on the other
415 hand, are two conceptually different ways of thinking about meridional transport and the
416 MOC in the North Atlantic (see e.g. Hughes et al. 2012). As an example T_W provides
417 no detailed information on water mass variability which directly measured transports can
418 provide (Peña-Molino et al. 2011).

419 5. Results on correlation, coherence and group delay

420 We first investigate the relationships between the bottom pressure time series from lines
421 A, B and W (Fig. 4a) between 2004 and 2008. Then we investigate the relationship between
422 the integrated pressure gradient time series at lines B and W.

423 a. *Pressure time series: fast barotropic waves propagation*

424 The pressure records are strongly correlated all across the WAVE array. For the two
425 periods of overlapping single deployments delineated by vertical dashed lines in Fig.4a, the
426 strongest correlation (0.96) is found between B3 and B4 for the 2006-2007 time period, and
427 the weakest correlation (0.61) is found for the same time period between W2 and B5. Close

428 examinations of the time series reveal that various short time delays exist between all time
429 series. Cross-spectral analyses (not shown) shows that the coherence squared is close to one
430 for sub-inertial frequencies but decreases at super-inertial frequencies, and also towards the
431 zero frequency. The lack of coherence at low frequencies is partly ascribable to the various
432 instrumental drifts and the unique corrections applied to each record.

433 Group delays between all BPR records were estimated for two time periods: August
434 2004 to August 2006, and August 2006 to October 2007. Within each interval, the longest
435 overlapping period between BPR pairs was used. The details of the signal processing method
436 are given in the Appendix, but conceptually the method consists in estimating the derivative
437 of the phase of the cross spectra with respect to frequency, which is the group delay (Hannan
438 and Thomson 1973). The method allows for selection of the frequency range over which to
439 conduct the procedure, and estimation of delays which are not necessarily an integer multiple
440 of the time step of the time series, and possibly shorter. In contrast, conventional lagged
441 correlation methods integrate over all frequencies irrespective of the signal-to-noise level, and
442 can only provide estimates which are multiples of the time step. The range of frequencies over
443 which the estimation is conducted is chosen here to correspond to sub-inertial frequencies,
444 where the coherence is the largest.

445 The group delay estimates (Fig. 11) are not formally statistically different from zero
446 according to 95% confidence intervals based on two standard deviations of the formal dis-
447 tribution of the estimates (see Appendix). Despite this, a general pattern emerges with
448 25 delays out of the 28 estimated indicating that pressure signals propagates equatorward
449 along the boundary from lines A to B to W. Three delays only indicate signals propagating
450 northward, with one corresponding to an unphysical speed and extracted from one of the

451 noisiest records. Within each line, signals are found to propagate either upslope or downs-
452 lope with no consistent direction. With approximate distances between the lines following
453 the 2000 m depth isobath being 932 km from Line A to Line B and 990 km from Line B to
454 Line W, the delays between lines correspond to a range of propagation speeds of 138–839
455 m s^{-1} between Line A and Line B, and 128–675 m s^{-1} between Line B and Line W. One
456 delay estimate from B2 to W1 implies a 2196 m s^{-1} speed. Apart from this last outstanding
457 value, the speeds and most observed directions of propagation between arrays are consis-
458 tent with expectations based on barotropic wave mode calculations using a two-dimensional
459 model with realistic topographic profiles from this region conducted by O’Rourke (2009).
460 She found the gravest mode wave speed in the range 170 - 220 m s^{-1} (highlighted by shading
461 in Fig. 11), corresponding to a barotropic Kelvin wave mode of lengthscale of order 2000
462 km perpendicular to the coast, therefore almost independent of depth over the continental
463 slope, as observed here (since lags within each array are relatively small except lags calcu-
464 lated from B0 in 2006-2007 which are clearly anomalous). Similar in-phase bottom pressure
465 perturbations were observed from the MODE bottom experiment between sites hundreds of
466 km apart near 28°N in the North Atlantic (Brown et al. 1975). These coherent, barotropic
467 signals may also be responsible for the coherent sea level signals seen in satellite altimetry
468 on the global continental slope (Hughes and Meredith 2006).

469 Assuming no variability on the eastern boundary, depth-independent pressure fluctua-
470 tions on the western boundary would, from (1) be associated with a net meridional geostrophic
471 flow across the latitude of the observations. At the latitude of lines A and B, a pressure
472 anomaly p'_W of 1 mbar would produce a transport anomaly of $H p'_W / (\rho f)$ of 5 Sv assuming
473 a depth $H = 5000$ m. With a typical standard deviation of 2.5 mbar in the observations,

474 this produces 12.5 Sv standard deviation in the transports. The rapid propagation speeds
475 estimated here imply that these perturbations are transmitted along the continental slope
476 between 38°N and 43°N almost instantaneously (in a matter of hours) compared to their
477 time scale (2.5 days, as estimated from the first spectral moment of a typical BPR record
478 from Fig.4a). It is likely that these adjustments are actually balanced rapidly by very sim-
479 ilar pressure perturbations on the eastern boundary at the same latitudes but we have no
480 way of assessing this. Such compensation was actually observed by Bryden et al. (2009) in
481 boundary pressure records across 26°N in the Atlantic Ocean. If this also occurs at our lati-
482 tudes, any net northward transports associated with these barotropic pressure perturbations
483 are likely to be smaller than the 12.5 Sv number estimated above when the eastern bound-
484 ary is constant. Nevertheless, these perturbations still produce net meridional transports
485 across latitudes, on synoptic atmospheric time scales associated with global oscillations of
486 masses between ocean basins (Stepanov and Hughes 2006). Detection of these signals, and
487 their spatial coherence over large distances, demonstrates that the instruments are produc-
488 ing good quality data and are capable of detecting propagating signals. Their relevance for
489 overturning processes, however, is small. Thus, we turn to the analysis of the layer transport
490 time series derived from the pressure gradients, which are directly linked theoretically to the
491 overturning processes in (2).

492 *b. Pressure gradient time series: waves or advection?*

493 The two time series of integrated pressure gradients T_B and T_W overlap for 1325 days
494 (Fig. 12). They are correlated at 0.18 with a p-value associated with the test statistic of

495 Ebisuzaki (1997) equal to 0.0046. The correlation after 30-day lowpass filtering of the time
496 series is larger, at 0.32, with a p-value of 0.0018. These significant levels of correlation are a
497 validation of our methods, and an indication that the pressure gradients reconstructed at Line
498 W and at Line B both capture a common signal which is large-scale. Such boundary signals
499 were also found in OGCMs where they were related to overturning transport processes, in
500 agreement with (2) (Roussenov et al. 2008; Bingham and Hughes 2008).

501 The variability of T_B and T_W and their co-variability as a function of frequency is exam-
502 ined by a cross spectral analysis summarized in Fig. 13. The multitaper method used (see
503 Appendix) allows us to obtain spectral estimates at the period corresponding to the com-
504 mon length of the time series. Between periods of about 11 days and 90 days, the spectra
505 are very similar apart from a strong peak at Line W near 34 days (Fig. 13a). Topographic
506 Rossby waves have been identified as the major source of variability over a range of periods
507 from about 1 to 3 weeks, in deep current meter measurements along the WAVE array region
508 (Rhines 1971; Thompson 1971; Thompson and Luyten 1976; Louis et al. 1982; Shaw and
509 Csanady 1988; Hogg 2000), and are usually ascribed to radiation from eddies interacting
510 with topography, so it is to be expected that part of the variability will be quite localised.
511 The 34-day peak at Line W may be an example of this, although it is at longer period. The
512 low power at Line B for periods longer than 6 months probably results from the removal of
513 low frequency power when detrending the BPR data. The Line B spectrum is also noticeably
514 quieter than Line W at periods shorter than about 9 days, in contrast to the currents near
515 Line A (Hogg, 2000), which show enhanced energy at periods around 4 days.

516 The covariance between T_B and T_W occurs predominantly at low frequencies: at periods
517 shorter than 10 days approximately, the power has decreased by two orders of magnitude

518 compared to the low frequencies, and the coherence squared is generally low (Fig. 13b). The
519 time scales where the coherence squared is continuously significant seem limited to periods
520 longer than approximately 85 days, reaching values greater than 0.7. At these time scales
521 the phase estimates are near zero with no obvious dependence on frequency (Fig. 13c). High
522 coherence squared also appears over much of the range between periods of about 30 and 80
523 days.

524 In order to investigate two possible causes of the correlation and coherence of the two
525 time series, namely advection by the DWBC or propagation of boundary waves, we seek to
526 determine plausible time delays between the two time series. First, a straightforward lagged
527 cross correlation between the two time series peaks at 9 days with T_B leading T_W . However,
528 as the spectral and cross spectral analyses showed, we can think of these time series as an
529 aggregation of processes operating at different scales, and that the delay between processes
530 may depend on the frequency. Hence, aggregating across all frequencies will produce an
531 average delay which will exhibit biases for most frequencies. As such, we estimate constant
532 time delays for specific frequency ranges, or group delays. Based on the cross spectral analysis
533 and dynamical considerations, we select the following five frequency limits which define four
534 distinct frequency ranges of estimation, and six additional combined ranges. The first limit is
535 $1/708$ cpd which corresponds to the longest single deployment of BPRs at Line B. The second
536 limit is $1/180$ cpd which is an approximate upper limit for the frequencies which are affected
537 by BPR drift corrections (not shown), as well as a change in power of the T_W spectrum.
538 The third limit is $1/90$ cpd as it corresponds to a significant drop in the spectrum of T_B , as
539 well as in the cross spectrum and coherence squared, and an apparent change of behavior of
540 the coherence phase. The fourth limit is $1/30$ cpd because it marks another change in the

541 phase behavior and is past the very large peak centered at $1/34$ cpd in the T_W spectrum.
542 The fifth and final limit is $1/10$ cpd, because above this frequency ageostrophic variability in
543 pressure may become more important as was shown by the pressure reconstruction (Fig. 6).
544 Additionally, both cross spectrum and auto spectra become dramatically reduced, making
545 our model of constant group delay at these frequencies more vulnerable to biases in the
546 estimation method.

547 The group delays in the frequency ranges defined by these limits are listed in Fig. 14 with
548 95% confidence intervals, where negative values denote a signal propagation from Line B to
549 Line W. All estimates which include the $1/90$ – $1/30$ cpd range have nominal negative delays
550 between -10 and -12 days. The estimate in the $1/90$ – $1/30$ cpd range itself is -11 days but
551 the error bar is 46 days. The estimate in the $1/30$ – $1/10$ cpd range is -19 days but the error
552 bar is as large as the estimate itself. In contrast, the delay estimates at periods greater than
553 90 days are all clearly indistinguishable from zero, meaning that at these longer time scales
554 the two time series are essentially coincident in time. Interestingly, the nominal delays in
555 the individual ranges $1/708$ – $1/80$ cpd and $1/180$ – $1/90$ cpd are both positive, yet statistically
556 indistinguishable from zero.

557 All the calculated delays which are significantly different from zero are negative, between
558 -10 and -12 days, representing propagation from Line B to Line W as expected for CTWs.
559 This corresponds to speeds of between 0.95 and 1.15 m s^{-1} , although the wide error bars
560 imply speeds between about half and four times these values.

561 The most natural CTW mode to compare with is mode 1 (Fig. 2) because this mode has
562 the same monotonic structure of bottom pressure as a function of depth as that seen in the
563 observations. Yet, this mode has a propagation speed of over 5 m s^{-1} which is significantly

564 faster than that deduced from observations. The calculated wave speeds are both group and
565 phase speeds, as the modes are calculated in the non-dispersive, long-wave limit appropriate
566 to periods of tens of days or longer. Higher modes have lower speeds, but even mode 3
567 propagates at almost 1.5 m s^{-1} , and has an oscillatory structure in bottom pressure.

568 Thus we see that, while the signal propagation speeds are roughly similar in size to
569 expected wave speeds, they do seem to be significantly slower. This situation is reminiscent of
570 that discussed by Hallberg and Rhines (1996), in which forcing impinging on the continental
571 slope sets up a “topographic beta plume” flow of counter-propagating jets on the slope. The
572 flow develops along the path followed by topographically-influenced waves propagating in
573 the same sense as CTWs away from the forcing region, but it continues to develop after
574 the first waves have passed. While the waves are responsible for propagating information
575 along the continental slope from the forcing region, the continuing development of the flow
576 in the wake of the first waves may produce a slower propagation of the fully-developed “beta
577 plume” circulation.

578 In summary, we find significant coherence between Line B and Line W, for the depth-
579 dependent pressure mode which is expected to be associated with an overturning circulation.
580 We also find evidence for propagation of signals in the sense of CTWs, with a best estimate
581 for the speed of about 1 m s^{-1} . This appears to be rather slow for the expected CTW mode,
582 and may be indicative of the slower development of a topographically-controlled circulation
583 in the wake of propagating CTWs.

584 *c. Can the observed delays be explained by advective processes?*

585 An alternative source of correlation between the two sections is advection of density or
586 potential vorticity anomalies in the DWBC. The speeds discussed in the previous section
587 seem too large to be explained by such processes, but these speeds were only derived for a
588 subset of frequency ranges; other frequencies permit a wider range of speeds. This raises
589 the question of whether advective processes could be responsible for any of the observed
590 coherence.

591 Limiting our attention to signals propagating from Line B to Line W (i.e. negative
592 delays), the numbers in Fig. 14 show that the longest permitted delay is 112 days (corre-
593 sponding to 10 cm s^{-1} propagation speed). This lies in the 180–708 day period band for
594 which the Line B time series is least reliable. For all other bands, the longest permitted
595 delay is 67 days (17 cm s^{-1}), and the longest excluding the less reliable periods longer than
596 180 days is a 57-day delay (20 cm s^{-1}).

597 Tracer studies in this region (Holzer et al. 2010; van Sebille et al. 2011; Peña-Molino et al.
598 2011) suggest mean advection speeds of $1\text{--}3 \text{ cm s}^{-1}$, much slower than our observations would
599 imply. However, tracer studies produce an average over all routes, including the most direct
600 route in the DWBC as well as slower interior pathways, and both routes have been observed
601 (Bower et al. 2009, and references therein). Could there be a precursor advective signal
602 which takes the fastest route, and accounts for some of our observed correlations? Certainly,
603 near-bottom velocities in the region do approach the $10\text{--}20 \text{ cm s}^{-1}$ speeds which are at the
604 limit of acceptability in our data (e.g. Shay et al. 1995; Bower and Hunt 2000; Pickart and
605 Watts 1990). We investigate this in more detail, using independent Lagrangian data, and

606 Eulerian data from Line W.

607 1) LAGRANGIAN ASSESSMENT

608 First we consider 25 acoustically-tracked RAFOS floats released in the DWBC between
609 the Grand Banks and Cape Hatteras in 1994 and 1995 for the BOUNCE experiment (Bower
610 and Hunt 2000). The floats, drifting at pressure levels between 3000 and 3600 db (deep) or
611 between 900 and 1500 db (shallow), showed mean advective rates equatorward at 2–5 cm
612 s^{-1} along the western boundary. Nine of the deep floats (Fig. 15a) crossed perpendicularly
613 first Line B and then Line W, all with advective times longer than 57 days (Fig. 15b). Of
614 these floats, two (b262 and b280) traveled the distance in 94 and 96 days, which is shorter
615 than the 112-day limit diagnosed earlier for the 708-day to 6-month band of periods. The
616 slowest deep float (b265) took 480 days but this occurred because it recirculated before being
617 recaptured by the DWBC. Three shallow floats were released upstream or very close to Line
618 B and drifted eventually past Line W. Two other shallow floats were released downstream or
619 near Line W but were advected first northeast by the Gulf Stream before being recaptured
620 by the DWBC, eventually crossing Line B and Line W. The advection times for these shallow
621 floats varied from 121 days to 512 days, all longer than the 57-, 67- or even 112-day limits
622 (Fig. 15d).

623 One may ask if the strength or the structure of the DWBC during BOUNCE was repre-
624 sentative of the strength of the DWBC during our time series of pressure gradient. As such
625 we also consider the 76 RAFOS floats from the ExPath experiment, which were released in
626 the DWBC near 50°N between 2003 and 2006 at 700 m and 1500 m depth (Bower et al.

627 2009). These floats tracking the recently ventilated Labrador Sea Water entered the sub-
628 tropics via the interior of the gyre, not the DWBC. Only two floats, one shallow and one
629 deep, were advected past Line B within the DWBC (Fig. 15a,b and see also Fig. 1 in Bower
630 et al. (2009)). The shallow float e667 crossed Line B around 16 October 2006 and reached
631 approximately Line W 129 days later on 24 February 2007, mostly following the 1000 m
632 isobath. The deep float e442 passed Line B around 20 July 2007, and reached approximately
633 mid-distance between Line B and Line W in about 99 days, following for the most part
634 the 3000 m isobath. The advection times from these two more recent floats are therefore
635 consistent with the ones deduced from the earlier BOUNCE floats.

636 In conclusion no float from the BOUNCE or ExPath experiments traveled in the 57
637 days necessary to be within the error bars of observed delays at periods shorter than 180
638 days. However, the negative 112-day limit of the confidence intervals for the delay estimate
639 including time scales longer than 6 months is longer than the advective propagation times
640 diagnosed from two BOUNCE floats. This overall suggests that advection by the DWBC
641 could play a small role for the coherence on time scales longer than 6 months, but not on
642 shorter time scales.

643 2) EULERIAN ASSESSMENT

644 The limited number of Lagrangian floats available for study may not capture the fastest
645 possible advective route between lines B and W, but we can use Eulerian velocities to esti-
646 mate propagation times without the complication of possible detrainment from the DWBC.
647 Therefore, we consider the near-bottom along-slope velocity records from Line W which

648 were actually used to derived T_W (Fig. 5a). In fact it is near the bottom within the DWBC
649 that the largest southwestward mean velocities are found at Line W (see Figs. 2 and 3 of
650 Toole et al. (2011)), so these velocity records are the most favorable to produce a fast signal
651 propagation. We assume that these records are representative of the along-slope velocity on
652 the continental slope between Line B and Line W. While this is unrealistic, it is the fastest
653 signal propagation scenario that neglects recirculation and meanders of the DWBC which
654 are expected to lengthen the advection time. The velocity time series from the beginning of
655 the overlap period of T_W and T_B are integrated in time until the cumulative distance equals
656 990 km, and this is repeated with a start time every subsequent day. This is equivalent to
657 seeding particles at Line B every day in a DWBC with the velocity measured at Line W,
658 along 6 isobaths ranging from 1000 m to about 4000 m.

659 The results are displayed as histograms of advection times in Fig. 16. The median values
660 of those histograms range from 147 to 367 days. These fall outside the 95% confidence
661 intervals of the group delays of Fig. 14. However, advection times as short as 92 days occur
662 from the near-bottom velocity at mooring W4. The value -92 is within the 95% confidence
663 interval of the group delay estimate for the 708-day to 6-month band of periods. Yet, if
664 one notes that the left limit of this interval (-112) is at 2.5% of the associated cumulative
665 distribution function of the probability of the estimate, then -92 is still only at the 4.1% mark.
666 In other words, there is only a 4.1% probability that the true delay is equal or less than -92
667 days. A 92-day propagation implies a mean advection speed greater than 0.12 m s^{-1} . This
668 appears to be a period of relatively vigorous mean flow compared to other measurements
669 of near-bottom velocities in this region. At the RAPID-Scotian Line (Hughes et al. 2012),
670 the successor to Line B deployed in 2008, near-bottom records showed along-slope currents

671 with extremes in the range 0.13–0.32 m s⁻¹ depending on locations on the slope, yet the
672 one-year-average along-slope current was in the range 0.01–0.05 m s⁻¹. Others such as Shay
673 et al. (1995) reported extremes of velocity near 0.40 m s⁻¹ at 3500 m depth on moorings of
674 the SYNOP experiment in the vicinity of Line W, yet the mean for 26 months was only 0.07
675 m s⁻¹ towards the southwest. Line W records at W4 indicated also extremes at 0.39 cm s⁻¹.

676 In conclusion, the analysis of Lagrangian and Eulerian velocity datasets suggest that that
677 advection in the DWBC is too slow to account for the coherence at time scales shorter than
678 six months. At longer periods advection cannot be excluded as a factor, but appears to be
679 unlikely to account for the coherent signals seen here. We would expect advection in the
680 DWBC or via diffusive pathways to play an increasing role at multi-year to decadal time
681 scales (e.g. van Sebille et al. 2011; Peña-Molino et al. 2011; Holzer et al. 2010).

682 **6. Summary and concluding remarks**

683 Observations of bottom pressures collected between 2004 and 2008 as part of RAPID
684 WAVE on the western boundary of the North Atlantic were analyzed. This analysis included
685 using boundary pressure gradient observations integrated to yield time series of western
686 boundary contribution to basin-wide zonally-integrated meridional transports, an approach
687 shown to be successful in an OGCM (Bingham and Hughes 2008), to test the hypothesis that
688 transport anomalies are communicated along the western boundary of the North Atlantic.

689 First, the analysis of detided BPR pressure records revealed the existence of signals
690 propagating at speed of at least 128 m s⁻¹ from northeast to southwest, in the general
691 orientation of the axis formed by lines A, B and W along the western boundary slope

692 between approximately 43°N and 38°N. These signals were attributed to near-barotropic
693 coastally-trapped waves propagating basin-scale disturbances excited by atmospheric forcing
694 or oscillation of mass between ocean basins. Yet, these pressure oscillations were observed
695 to be relatively independent of depth and are of little relevance for meridional overturning
696 processes.

697 Second, the analysis of the covariance at time scales shorter than 3 months of the two
698 time series of western boundary contribution to meridional transports suggested that pressure
699 gradient signals propagate from Line B to Line W in between 3 to 21 days. The nominal
700 delay of propagation is on average 11 days which corresponds to a propagation speed of
701 about 1 m s⁻¹. Such speed is roughly consistent with CTW speeds, but seems rather slow
702 when compared with the realistic topography study of O’Rourke (2009).

703 Additionally, the two transport time series are systematically significantly coherent for
704 time scales longer than three months and nearly in phase. The examination of acoustically-
705 tracked float trajectories and Eulerian velocity records at Line W showed that the DWBC
706 is too slow to propagate anomalies which could account for the observed coherence phase
707 on time scales between three and six months. There is a small chance that advection in the
708 DWBC could account for the observed coherence phase on longer time scales, but the ad-
709 vective mechanism seems most relevant at timescales longer than those amenable to analysis
710 in our dataset.

711 The separate investigations of coherence by advection of the DWBC on one hand and
712 the propagation of long wavelength CTW on the other hand may be a simplistic approach.
713 Indeed, the investigations of O’Rourke (2009) neglected the possible influence of the mean
714 flow on wave propagation, namely here the DWBC and the surface-intensified Gulf Stream,

715 which could act to speed up or slow down the wave speeds. Many observations within the
716 DWBC in this region provide evidence for the superposition, if not the interactions, of waves
717 and DWBC flows. A velocity section taken during the BOUNCE experiment near our Line
718 B showed a banded structure which was associated with TRW (Bower and Hunt 2000). The
719 section of mean velocity at Line W reported by Toole et al. (2011) also showed such a banded
720 structure. Near 35°N on the western boundary, Pickart and Watts (1990) found it necessary
721 to extract a dominant part of the variance in velocity signals associated with waves, in order
722 to quantify the underlying low frequency DWBC fluctuations. Finally the waves themselves
723 could be responsible for setting up the DWBC in the manner described by Hallberg and
724 Rhines (1996) using an idealized 2-layer model. In this model, convectively-driven forcing
725 leads to a “topographic beta plume” response in the form of currents and pressure changes
726 which form in the wake of TRWs as they propagate along the sloping western boundary away
727 from the forcing region. Development of the currents behind the TRW could also account
728 for the relatively slow propagation speeds found here.

729 While it is clear that the correlations we observe do not result from advective processes,
730 the simple explanation in terms of CTW does not seem to be entirely satisfactory either, as
731 the wave speed does not match expectations. Further investigations using high resolution
732 numerical modeling would help to disentangle the correlated signal from the various localized
733 effects which might also be expected in this region. Such effects are evident in the different
734 levels found in the power spectra of T_W and T_B near 34 days time scale in Fig. 13a. Line W
735 seems to capture much more variance associated with what is usually recognized to be TRWs
736 activity in this region, traditionally attributed to wave radiation from the Gulf Stream and
737 its rings (e.g. Pickart 1995).

738 This present study has not explored another possible source of coherence between the
739 two transport time series which is that the correlation and coherence result from spatial
740 correlation in an external forcing such as atmospheric pressure or wind stress. This will be
741 investigated elsewhere.

742 *Acknowledgments.*

743 This work was funded by the UK Natural Environment Research Council. Sofia Olhede
744 was supported by EPSRC grant EP/I005250/1. Initial observations at Station W (20012004)
745 were made possible by a grant from the G. Unger Vetlesen Foundation and support from the
746 Woods Hole Oceanographic Institution. Since 2004, the Line W program has been supported
747 by the US National Science Foundation with supplemental contribution from WHOIs Ocean
748 and Climate Change Institute. The authors would like to thank Amy Bower for providing
749 the BOUNCE and ExPath float data which made an extremely valuable contribution to
750 this study. The authors would like to thank Miguel Angel Morales Maqueda for assistance
751 with the deployment and recovery of the data. We thank Eleanor O'Rourke for the use of
752 her Ph.D. dissertation results and the adaptation of her figure for Fig. 2. Comments by
753 Eleanor Frajka-Williams, Richard Williams improved the final manuscript. We thank Peter
754 Rhines and an anonymous reviewer for their useful suggestions which improved the final
755 manuscript.

757 Spectral estimation

758 Cross spectral density functions between random variables $x(n)$ and $y(n)$ with zero means
759 are estimated using multi-taper estimates (Percival and Walden 1993)

$$760 \quad \hat{S}_{xy}(\nu) \equiv \frac{1}{K} \sum_{k=1}^K \hat{S}_{xy}^k(\nu) \quad \text{with} \quad (A1)$$

$$761 \quad \hat{S}_{xy}^k \equiv \Delta t \left(\sum_{n=1}^N h^k(n)x(n)e^{-i2\pi\nu n\Delta t} \right)^* \times \left(\sum_{n=1}^N h^k(n)y(n)e^{-i2\pi\nu n\Delta t} \right), \quad (A2)$$

762 where ν is frequency, $(.)^*$ designates the complex conjugate, N is the number of points in
763 the time series, and $h^k(n), n = 1, 2, \dots, N$ is the k th discrete prolate spheroidal sequence
764 with half time-bandwidth parameter NW and order $k = 1, \dots, K$. In order to obtain smooth
765 estimates, here $NW = 4$ and $K = 2NW - 1$ are chosen. Coherence squared and coherence
766 phase estimates are computed as

$$767 \quad \frac{|\hat{S}_{xy}|^2(\nu)}{\hat{S}_{xx}(\nu)\hat{S}_{yy}(\nu)}, \quad \arg(\hat{S}_{xy}(\nu)). \quad (A3)$$

768 Group or time delay estimation

769 If a signal $x(t)$ is captured with a constant delay D as $y(t - D)$ then the theoretical cross
770 spectrum between them is $S_{xy}(\nu) = S_{xx}(\nu)e^{-i2\pi\nu D}$, and the phase of the cross-spectrum is
771 a linear function of frequency. The group delay estimation method of Hannan and Thom-
772 son (1973) consists of implementing a method to obtain an estimate of D based on this
773 expectation of the cross-spectrum.

774 An estimate $\hat{S}_{xy}(\nu)$ of the true cross spectrum can be written as

$$775 \quad \hat{S}_{xy}(\nu) = |\hat{S}_{xy}(\nu)|e^{i\hat{\theta}(\nu)}, \quad (\text{A4})$$

776 where $\hat{\theta}(\nu)$ is the cross spectrum phase or coherence phase. Next, a band of frequencies B
 777 which contains M fundamental frequencies $1/(N\Delta t)$ is chosen, and the following quantity is
 778 computed

$$779 \quad \hat{p}(D) = \frac{1}{M} \sum_{m=1}^M \hat{S}_{xy}^1(\nu_m) e^{-i2\pi\nu_m D} \quad (\text{A5})$$

$$780 \quad = \frac{1}{M} \sum_{m=1}^M |\hat{S}_{xy}^1(\nu_m)| e^{i[\theta(\nu_m) - 2\pi\nu_m D]}, \quad \nu_m \in B \quad (\text{A6})$$

781 where only one taper (the first prolate spheroidal sequence) is used to form the cross spectral
 782 estimate $\hat{S}_{xy}^1(\nu_m)$. No more smoothing of the cross spectral is required as the frequency
 783 smoothing operation is done by the choice of the band B . D is assumed to be a constant
 784 delay in the frequency band B and an estimate is produced for each B . The group delay
 785 estimate \hat{D} is the value which maximizes $\hat{q}(D) = |\hat{p}(D)|^2$, which is found by a standard
 786 minimization routine on $-\hat{q}$.

787 Once \hat{D} is obtained, uncertainties in the estimates are computed by considering the
 788 estimated maximized coherence squared in band B

$$789 \quad \hat{\sigma}_B^2 = \frac{q(\hat{D})}{\hat{S}_{xx}^1 \hat{S}_{yy}^1}, \quad (\text{A7})$$

790 which can be used to substitute for the true σ_B^2 in the following expression for the variance
 791 of \hat{D} :

$$792 \quad \text{Var}[\hat{D}] = \frac{3N^2}{M^3} \frac{1 - \sigma_B^2}{2\pi\sigma_B^2}. \quad (\text{A8})$$

793 Note that (A7) corrects the typographic error in equation (4) of Hannan and Thomson (1973)
 794 which has a square root for the denominator. Expression (A8) with (A7) is used to derive

795 95% confidence intervals assuming a normal distribution of the estimates:

$$796 \quad \hat{D} \pm 1.96 \left(\frac{3N^2}{M^3} \frac{1 - \hat{\sigma}_B^2}{2\pi\hat{\sigma}_B^2} \right)^{1/2}. \quad (\text{A9})$$

797 Note that (A8) indicates that $\text{Var}[\hat{D}]$ increases with the length N of the time series but
798 decreases with the width of B . However, choosing a width too large for B may introduce
799 biases by including frequencies bands where a constant group delay may not be a good model
800 for the data.

801

REFERENCES

802

803 Bingham, R. and C. Hughes, 2008: Determining North Atlantic meridional transport vari-
804 ability from pressure on the western boundary: a model investigation. *J. Geophys. Res.*,
805 **113 (C09008)**, doi:10.1029/2007JC004679.

806 Bingham, R., C. Hughes, V. Roussenov, and R. Williams, 2007: Meridional coherence of
807 the North Atlantic meridional overturning circulation. *Geophys. Res. Lett.*, **34**, L23 606,
808 doi:10.1029/2007GL031731.

809 Bower, A. and H. Hunt, 2000: Lagrangian observations of the deep western boundary current
810 in the North Atlantic Ocean. Part I: Large-Scale Pathways and Spreading Rates. *J. Phys.*
811 *Oceanogr.*, **30 (5)**, 764–783.

812 Bower, A., M. Lozier, S. Gary, and C. Böning, 2009: Interior pathways of the north Atlantic
813 meridional overturning circulation. *Nature*, **459 (7244)**, 243–247.

814 Brink, K. and D. Chapman, 1985: Programs for computing properties of coastal trapped
815 waves and wind-driven motions over the continental shelf and slope. Tech. Rep. WHOI-
816 85-17, Woods Hole Oceanographic Institution, 45 pp.

817 Brown, W., W. Munk, F. Snodgrass, H. Mofjeld, and B. Zetler, 1975: MODE bottom
818 experiment. *J. Phys. Oceanogr.*, **5 (1)**, 75–85.

- 819 Bryden, H., A. Mujahid, S. Cunningham, and T. Kanzow, 2009: Adjustment of the basin-
820 scale circulation at 26°N to variations in Gulf Stream, deep western boundary current and
821 Ekman transports as observed by the RAPID array. *Ocean Sci.*, **5**, 421–433.
- 822 Chelton, D., R. Deszoeke, M. Schlax, K. El Naggar, and N. Siwertz, 1998: Geographical
823 variability of the first baroclinic Rossby radius of deformation. *J. Phys. Oceanogr.*, **28** (3),
824 433–460.
- 825 Chidichimo, M., T. Kanzow, S. Cunningham, W. Johns, and J. Marotzke, 2010: The con-
826 tribution of eastern-boundary density variations to the Atlantic meridional overturning
827 circulation at 26.5° N. *Ocean Sci.*, **6** (2), 475–490.
- 828 Cunningham, S., et al., 2007: Temporal variability of the Atlantic meridional overturning
829 circulation at 26.5°N. *Science*, **317** (5840), 935.
- 830 Ebisuzaki, W., 1997: A method to estimate the statistical significance of a correlation when
831 the data are serially correlated. *J. Clim.*, **10** (9), 2147–2153.
- 832 Hallberg, R. and P. Rhines, 1996: Buoyancy-driven circulation in an ocean basin with isopy-
833 cnals intersecting the sloping boundary. *J. Phys. Oceanogr.*, **26** (6), 913–940.
- 834 Hannan, E. and P. Thomson, 1973: Estimating group delay. *Biometrika*, **60** (2), 241.
- 835 Hogg, N. G., 2000: Low-frequency variability on the western flanks of the Grand Banks. *J.*
836 *Mar. Res.*, **58** (4), 523–545.
- 837 Holzer, M., F. Primeau, W. Smethie Jr, and S. Khatiwala, 2010: Where and how long ago

838 was water in the western North Atlantic ventilated? Maximum entropy inversions of bottle
839 data from WOCE line A20. *J. Geophys. Res.*, **115**, C07005, doi:10.1029/2009JC005750.

840 Hughes, C. and M. Meredith, 2006: Coherent sea-level fluctuations along the global conti-
841 nental slope. *Philos. Trans. R. Soc., A*, **364 (1841)**, 885–901.

842 Hughes, C. W., S. Elipot, M. A. Morales Maqueda, and J. Loder, 2012: Test of a Method
843 for Monitoring the Geostrophic Meridional Overturning Circulation Using Only Boundary
844 Measurements. *J. Atmos. Oceanic Technol.*, submitted.

845 Huthnance, J., 1978: On coastal trapped waves: Analysis and numerical calculation by
846 inverse iteration. *J. Phys. Oceanogr.*, **8 (1)**, 74–92.

847 IOC, IHO, and BODC, 2003: Centenary edition of the GEBCO digital atlas.

848 Johnson, H. and D. Marshall, 2002: A theory for the surface Atlantic response to thermo-
849 haline variability. *J. Phys. Oceanogr.*, **32 (4)**, 1121–1132.

850 Kanzow, T., et al., 2010: Seasonal variability of the Atlantic meridional overturning circu-
851 lation at 26.5°N. *J. Clim.*, **23**, 5678–5698, doi:10.1175/2010JCLI3389.1.

852 Louis, J., B. Petrie, and P. Smith, 1982: Observations of topographic rossby waves on the
853 continental margin off Nova Scotia. *J. Phys. Oceanogr.*, **12 (1)**, 47–55.

854 Lozier, M., W. Owens, and R. Curry, 1995: The climatology of the North Atlantic. *Progr.*
855 *Oceanogr.*, **36 (1)**, 1–44.

856 O’Rourke, E. A., 2009: The effect of topography on thermohaline adjustment. Ph.D. thesis,
857 University of Liverpool, 191 pp.

- 858 Peña-Molino, B., T. Joyce, and J. Toole, 2011: Recent changes in the Labrador Sea Water
859 within the Deep Western Boundary Current southeast of Cape Cod. *Deep Sea Res., Part*
860 *I*, **58 (10)**, 1019–1030, doi:10.1016/j.dsr.2011.07.006.
- 861 Percival, D. B. and A. T. Walden, 1993: *Spectral Analysis for Physical Applications*. Cam-
862 bridge University Press, Cambridge, UK.
- 863 Pickart, R., 1995: Gulf stream-generated topographic Rossby waves. *J. Phys. Oceanogr.*,
864 **25 (4)**, 574–586.
- 865 Pickart, R. and D. Watts, 1990: Deep western boundary current variability at Cape Hatteras.
866 *J. Mar. Res.*, **48 (4)**, 765–791.
- 867 Rhines, P., 1970: Edge-, bottom-, and Rossby waves in a rotating stratified fluid. *Geophys.*
868 *Astrophys. Fluid Dyn.*, **1 (3-4)**, 273–302.
- 869 Rhines, P., 1971: A note on long-period motions at Site D. *Deep-Sea Res.*, **18 (1)**, 21–26.
- 870 Roussenov, V., R. Williams, C. Hughes, and R. Bingham, 2008: Boundary wave commu-
871 nication of bottom pressure and overturning changes for the North Atlantic. *J. Geophys.*
872 *Res.*, **113 (C8)**, C08 042, doi:10.1029/2007JC004501.
- 873 Shaw, P.-T. and G. T. Csanady, 1988: Topographic waves over the continental slope. *J.*
874 *Phys. Oceanogr.*, **18 (6)**, 813–822.
- 875 Shay, T., J. Bane, D. Watts, and K. Tracey, 1995: Gulf Stream flow field and events near
876 68 W. *J. Geophys. Res.*, **100 (C11)**, 22 565–22 589.

- 877 Smith, W. H. F. and D. T. Sandwell, 1997: Global Sea Floor Topography from Satellite
878 Altimetry and Ship Depth Soundings. *Science*, **277** (5334), 1956–1962.
- 879 Stepanov, V. and C. Hughes, 2006: Propagation of signals in basin-scale ocean bottom
880 pressure from a barotropic model. *J. Geophys. Res.*, **111** (C12), C12002, doi:10.1029/
881 2005JC003450.
- 882 Thompson, R., 1971: Topographic Rossby waves at a site north of the Gulf Stream. *Deep*
883 *Sea Res.*, **18** (1), 1–19.
- 884 Thompson, R. and J. Luyten, 1976: Evidence for bottom-trapped topographic Rossby waves
885 from single moorings. *Deep-Sea Res.*, **23** (7), 629–635.
- 886 Toole, J., R. Curry, T. Joyce, M. McCartney, and B. Penã Molino, 2011: Transport of the
887 North Atlantic deep western boundary current about 39°N, 70°W: 2004-2008. *Deep-Sea*
888 *Res., Part II*, **58**, 1768–1780, doi:10.1016/j.dsr2.2010.10.058.
- 889 van Sebille, E., M. Baringer, W. Johns, C. Meinen, L. Beal, M. de Jong, and H. van Aken,
890 2011: Propagation pathways of classical labrador sea water from its source region to 26°N.
891 *J. Geophys. Res.*, **116** (C12), C12027, doi:doi:10.1029/2011JC007171.
- 892 Wang, D. and C. Mooers, 1976: Coastal trapped waves in a continuously stratified ocean.
893 *J. Phys. Oceanogr.*, **6** (6), 853–863.
- 894 Watts, D. and H. Kontoyiannis, 1990: Deep-ocean bottom pressure measurement: Drift
895 removal and performance. *J. Atmos. Oceanic Technol.*, **7** (2), 296–306.

- 896 Wright, D. and Z. Xu, 2004: Double Kelvin waves over Newfoundland shelf-break. *Atmos.-*
897 *Ocean*, **42**, 101–111.
- 898 Zhang, R., 2010: Latitudinal dependence of Atlantic meridional overturning circulation
899 (AMOC) variations. *Geophys. Res. Lett.*, **37 (L16703)**, doi:10.1029/2010GL044474.

900 List of Figures

- 901 1 Western North Atlantic bathymetry and locations of moorings at RAPID
902 WAVE Line A (A0 to A5) and Line B (B0 to B5), and moorings at Woods
903 Hole Line W (moorings are called here W0 to W5 for convenience). The
904 dashed line indicates the topographic section for which we report the results
905 of O'Rourke (2009) of baroclinic wave structure calculation. Bathymetry data
906 are from Smith and Sandwell (1997) topography database version 13.1. 52
- 907 2 Coastally-trapped wave solution modes 1, 2 and 3 for the baroclinic (stratified)
908 case for the topographic profile centered on 40.5°N (dashed line in Fig. 1).
909 The free wave form of the solutions is $\Psi(x, y, z, t) = \phi(x, z)e^{(ky - \omega t)}$ where
910 x is the coordinate or distance along the section, y the coordinate along the
911 continental slope, z the depth coordinate, k the wavenumber in the y direction,
912 ω the radian frequency, and t is the time variable. The solutions $\phi(x, z)$ are
913 presented for pressure, with arbitrary scaling for each panel. Zero contours
914 are drawn in white. The corresponding wave speed ω/k is indicated above
915 each panel. Adapted from O'Rourke (2009). 53

916 3 Vertical sections along WHOI Line W, Line B and Line A in their 2004 in-
917 strumental configuration. At Line W the vertical dashed lines are moorings
918 equipped with McLane profilers. Plus symbols are temperature and salinity
919 measuring instruments. Cross symbols are direct velocity measuring instru-
920 ments. The instruments on moorings used to derive bottom pressure gradients
921 are plotted in black. The rest of the instruments in gray are used to estimate
922 the transport across the array as in Toole et al. (2011). The black triangles
923 are bottom pressure recorders (BPR) used in this study as deployed in 2004.
924 The gray triangles are BPRs which records were not used in this study (They
925 were either not recovered or did not return usable data). At lines B and A
926 not all BPR records are available for the period 2004–2008. At Line A the
927 BPR with gray symbols were not recovered.

54

928 4 a) Western boundary pressure anomalies at Line A moorings A0 and A1,
929 Line W moorings W0 to W2, and Line B moorings B0 to B5. The second
930 recovered deployment at B5 plotted in gray exhibits larger variability at low
931 frequencies and was not used for this study. The time series are lowpass filtered
932 to retain periods longer than one day for this plot. b) EOF1 and c) EOF2 of
933 Line B boundary pressure records minus the shallowest records (with a zero
934 EOF amplitude by construction) for the three deployment periods 2004–2006,
935 2006–2007 and 2007–2008. The legend in each panel indicate the percentage
936 of variance explained by the modes for each time period. For comparison
937 purpose, the EOF1 amplitude in panel b) were scaled to align their slopes
938 between the depths of B2 and B3.

55

939 5 Records at WHOI Line W of a) along slope velocity and b) in-situ density
940 anomalies at 1000 m and the depth of W0 (1788 m) from the McLane profiler
941 at W1, and from near-bottom current meters at moorings W1 to W5. For
942 plotting purposes the time series at W1 to W5 were lowpass filtered to retain
943 periods longer than 1 day. 56

944 6 Analysis of bottom pressure difference Δp between moorings W2 and W1;
945 (a) from BPR data (black line) and reconstruction from density and veloc-
946 ity (gray line). Both time series are bandpass filtered to retain frequencies
947 between 1/90 and 1/7 cpd indicated by vertical dashed lines in (b) and (d).
948 (b) Coherence squared and (d) Coherence phase between the BPRs pressure
949 difference and the reconstructed pressure difference. In (b), the horizontal
950 dashed line indicates the 95% confidence level for coherence squared (the sig-
951 nificant level is valid at any fixed frequency). (c) Scatter plots of the filtered
952 reconstructed pressure differences (*y*-axis) and pressure differences from BPR
953 data (*x*-axis) at 12-hour intervals. In this last plot, the dashed lines are the
954 least squares fits to the scatter points (slope 0.74). For comparison, the solid
955 black lines is the slope 1, intercept 0 curve. 57

956 7 Western boundary bottom pressure analysis at Line W. (a) Time series of
 957 western pressure anomalies $-p'_W$ at the depths corresponding to the base
 958 of mooring W0 (top curve) to W5 (bottom curve), subsequently offset by
 959 20 mbar. Black and gray colors are alternated for legibility. One mbar is
 960 equivalent to a zonally-integrated northward volume transport of 1.08 Sv per
 961 km of depth, at this latitude. (b) First two EOF patterns of the pressure
 962 anomaly time series in (a) presented as a function of depth. The first mode
 963 explains 81.3% of the variance and the second mode 11.3%. 58

964 8 (a) T_W : western overturning transport time series between 1000 m and 4120
 965 m, relative to 1000 m. The gray line is the 12-h step time series and the black
 966 line is the 10-day lowpassed version. (b) T_{WEDGE} volume transport at Line
 967 W below 1000 m between the continental slope to the west and mooring W5
 968 to the east (see Fig. 3). Note the different scales between a) and b). 59

969 9 Time series of western pressure gradient $\partial p_W / \partial z$ at Line B in mbar km^{-1}
 970 (left axis); the right axis is labeled in equivalent transport unit in Sv since
 971 the pressure gradient is integrated to obtain the layer transport T_B in the
 972 1000 m to 4000 m depth range as $(\Delta z)^2 \partial p_W / \partial z / (2f\rho_0)$ with $\Delta z = 3000$ m,
 973 $f = 9.826 \times 10^{-5} \text{ s}^{-1}$, $\rho_0 = 1040 \text{ kg m}^{-3}$ (see text). 60

974 10 Left: schematic of an idealized configuration of barotropic overturning. A
975 current with uniform meridional velocity $v = -c$ flows over a continental
976 slope (gray shading) which occupies the west part of the domain from $x = 0$
977 to $x = 1$ and between $z = 0$ and $z = -1$. A barotropic current with velocity
978 $v = +c/(2\delta)$ of opposite sign flows over a flat bottom in the east part of the
979 domain from $x = 1$ to $x = 1 + \delta$. Right: depth profile of the corresponding
980 volume transport per unit depth $Q(z)$. 61

981 11 Relative delay estimates between BPR record pairs for the time period May
982 2004 to April 2006 in a) and for August 2006 to October 2007 in b). Because
983 these are relative delays for all pairs, values are plotted twice with opposite
984 signs. The same symbols are used in both panels when appropriate to denote
985 the delays estimated with respect to A0 (up pointing triangles), A1 (down
986 pointing triangles), B0 (circles), B1 (asterisks), B2 (crosses), B3 (pluses),
987 B4 (stars), B5 (diamonds), W0 (right pointing triangles), W1 (left pointing
988 triangles), and W2 (black triangles). The boxes shaded light gray indicate a
989 relative delay from Line A to lines B and W corresponding to a $170\text{--}220 \text{ m s}^{-1}$
990 expected range of speeds. The boxes shaded medium gray indicate relative
991 delays from Line B to lines A and W for the same speeds, and the boxes
992 shaded dark gray from Line W to lines B and A. As an example in the top
993 panel, it is estimated that a signal propagates from A0 to A1 in 40 min, from
994 A0 to B0 in 63 min, from A0 to B1 in 101 min etc. 62

995 12 T_B and T_W time series at 12-h intervals (gray lines). Both time series are
996 anomalies with zero mean but T_W is offset by -20 Sv for legibility. The thick
997 black curves are the 30-day lowpassed versions. 63

998 13 Spectral analysis between T_B and T_W using a 7 Slepian tapers spectral esti-
999 mate (Percival and Walden 1993). a) Auto spectral power density functions
1000 for T_B and T_W , and cross spectral density function between the two. The
1001 upper and lower limits of the formal 95% confidence intervals for the spectral
1002 density estimates based on the χ^2 probability distribution function with 7×2
1003 degrees of freedom imply on this linear scale to multiply the curves by 0.5
1004 and 2.5 approximately for each frequency value (these are not drawn for the
1005 legibility of the plot). b) Coherence squared. c) Coherence phase. The verti-
1006 cal dashed lines in all panels indicates the frequency limits which define the
1007 ranges in which the time delay estimations are conducted. A negative slope
1008 of the phase with frequency in c) indicates a possible propagation of a signal
1009 from Line B to Line W. 64

1010 14 Schematic of group delay estimates. These estimates are obtained for ranges
1011 of frequencies corresponding to the periods indicated at the top, also indicated
1012 in Fig. 13. Confidence intervals are at the 95% level. Group delay estimates
1013 which are different from zero according to the confidence intervals are in bold. 65

1014 15 a) Trajectories of deep RAFOS floats from the BOUNCE experiment which
1015 crossed perpendicularly both Line B and Line W (colored trajectories and
1016 square symbols at the launching locations) and one deep float from the ExPath
1017 experiment (black trajectory). The launching position of the ExPath float is
1018 outside of the map. The 1, 2, 3 and 4 km isobaths are contoured in gray. The
1019 locations of Line B and Line W moorings are indicated by black triangles.
1020 The corresponding advection times in days are reported on the horizontal
1021 scale below the map. b) Same than a) but for shallow floats of BOUNCE and
1022 one shallow float from ExPath which flowed in this region (black trajectory)
1023 but which launching position is outside of this region. 66

1024 16 Distribution of advection time scales between Line W and Line B based on
1025 integrating the velocity time series shown in 5a). 67

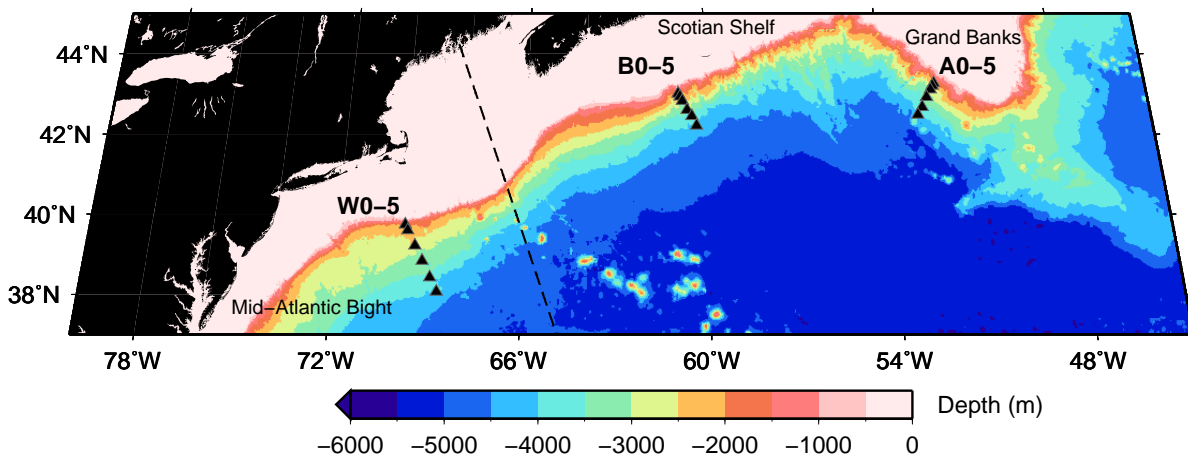


FIG. 1. Western North Atlantic bathymetry and locations of moorings at RAPID WAVE Line A (A0 to A5) and Line B (B0 to B5), and moorings at Woods Hole Line W (moorings are called here W0 to W5 for convenience). The dashed line indicates the topographic section for which we report the results of O'Rourke (2009) of baroclinic wave structure calculation. Bathymetry data are from Smith and Sandwell (1997) topography database version 13.1.

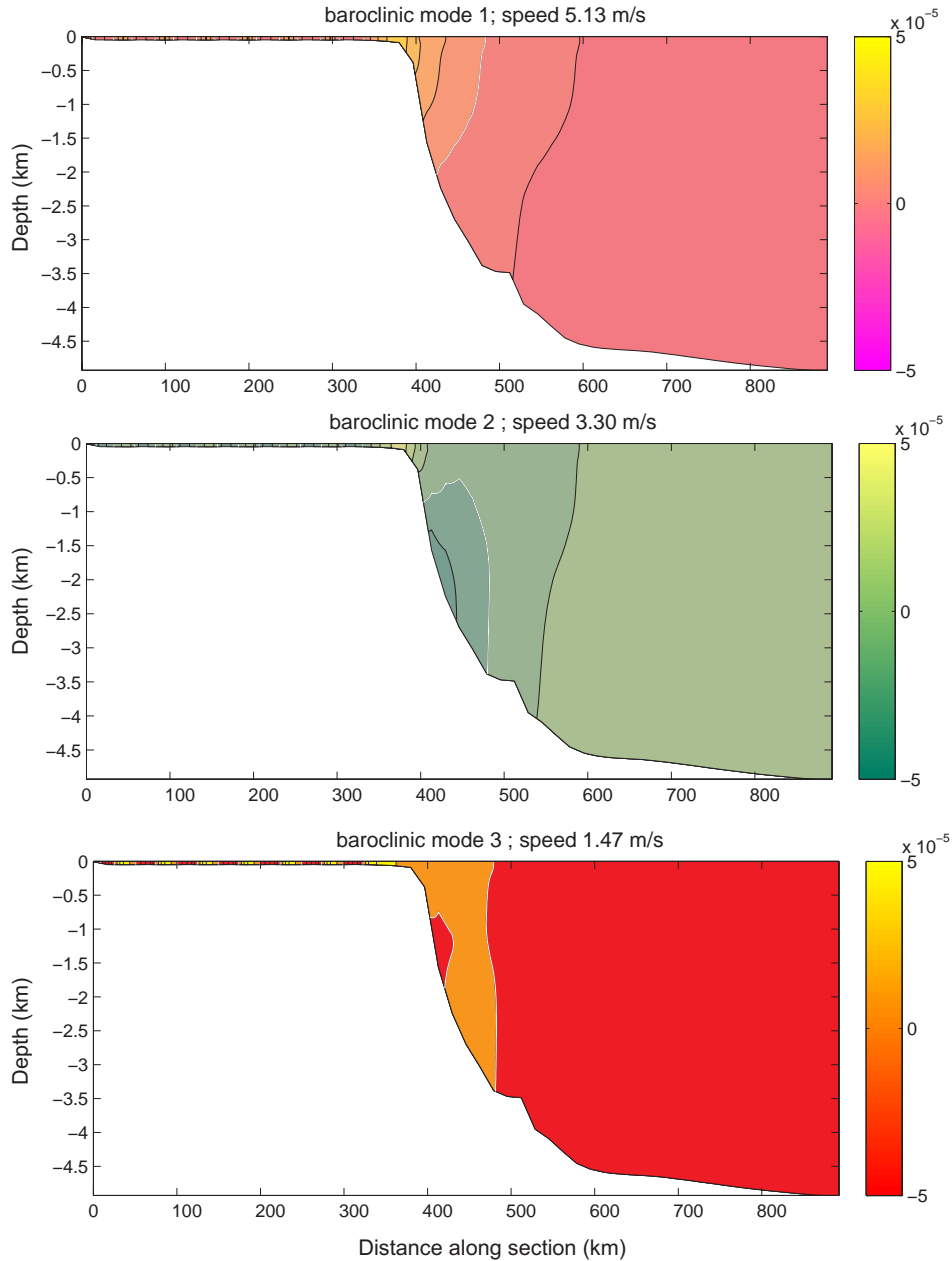


FIG. 2. Coastally-trapped wave solution modes 1, 2 and 3 for the baroclinic (stratified) case for the topographic profile centered on 40.5°N (dashed line in Fig. 1). The free wave form of the solutions is $\Psi(x, y, z, t) = \phi(x, z)e^{(ky - \omega t)}$ where x is the coordinate or distance along the section, y the coordinate along the continental slope, z the depth coordinate, k the wavenumber in the y direction, ω the radian frequency, and t is the time variable. The solutions $\phi(x, z)$ are presented for pressure, with arbitrary scaling for each panel. Zero contours are drawn in white. The corresponding wave speed ω/k is indicated above each panel. Adapted from O'Rourke (2009).

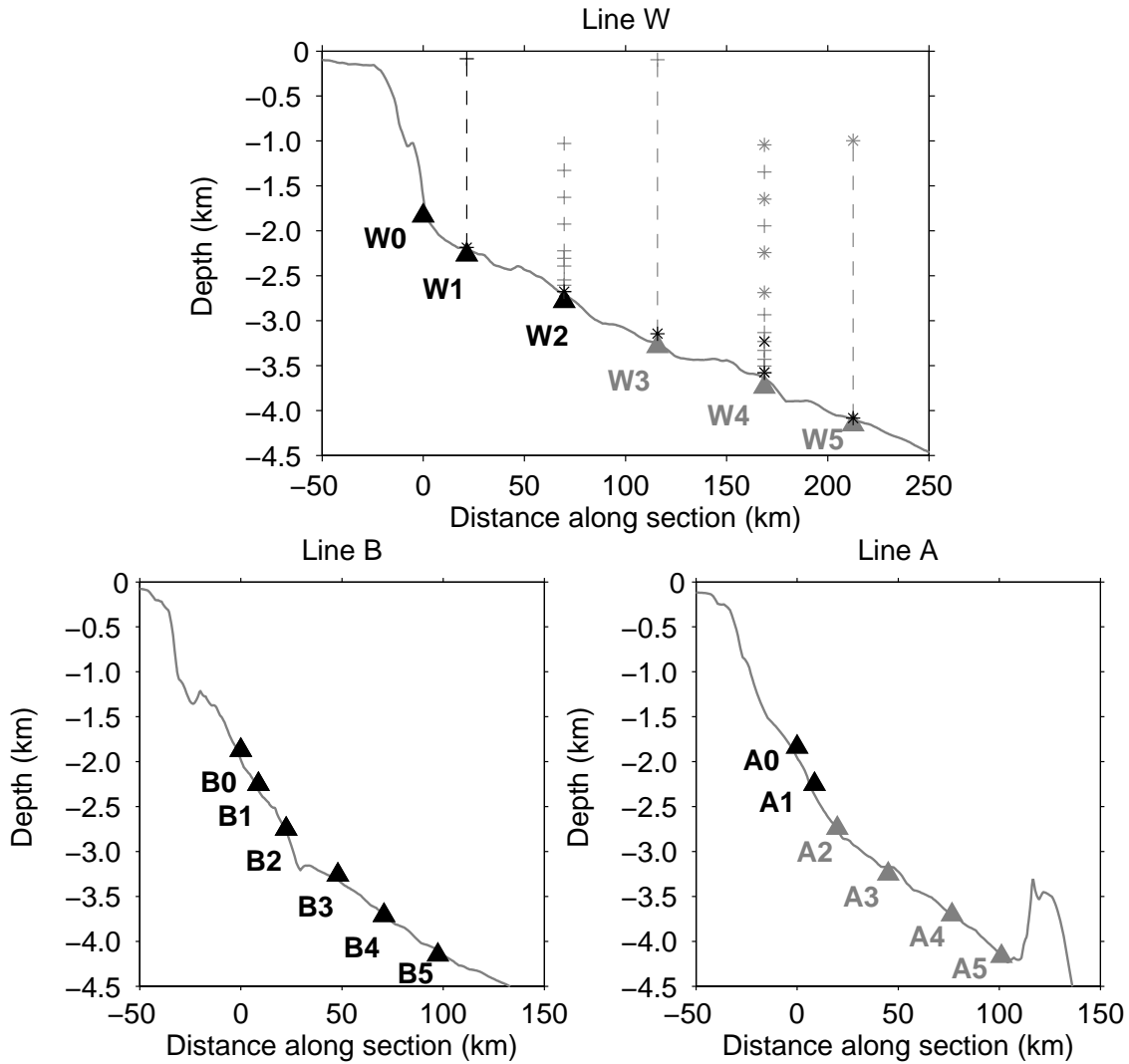


FIG. 3. Vertical sections along WHOI Line W, Line B and Line A in their 2004 instrumental configuration. At Line W the vertical dashed lines are moorings equipped with McLane profilers. Plus symbols are temperature and salinity measuring instruments. Cross symbols are direct velocity measuring instruments. The instruments on moorings used to derive bottom pressure gradients are plotted in black. The rest of the instruments in gray are used to estimate the transport across the array as in Toole et al. (2011). The black triangles are bottom pressure recorders (BPR) used in this study as deployed in 2004. The gray triangles are BPRs which records were not used in this study (They were either not recovered or did not return usable data). At lines B and A not all BPR records are available for the period 2004–2008. At Line A the BPR with gray symbols were not recovered.

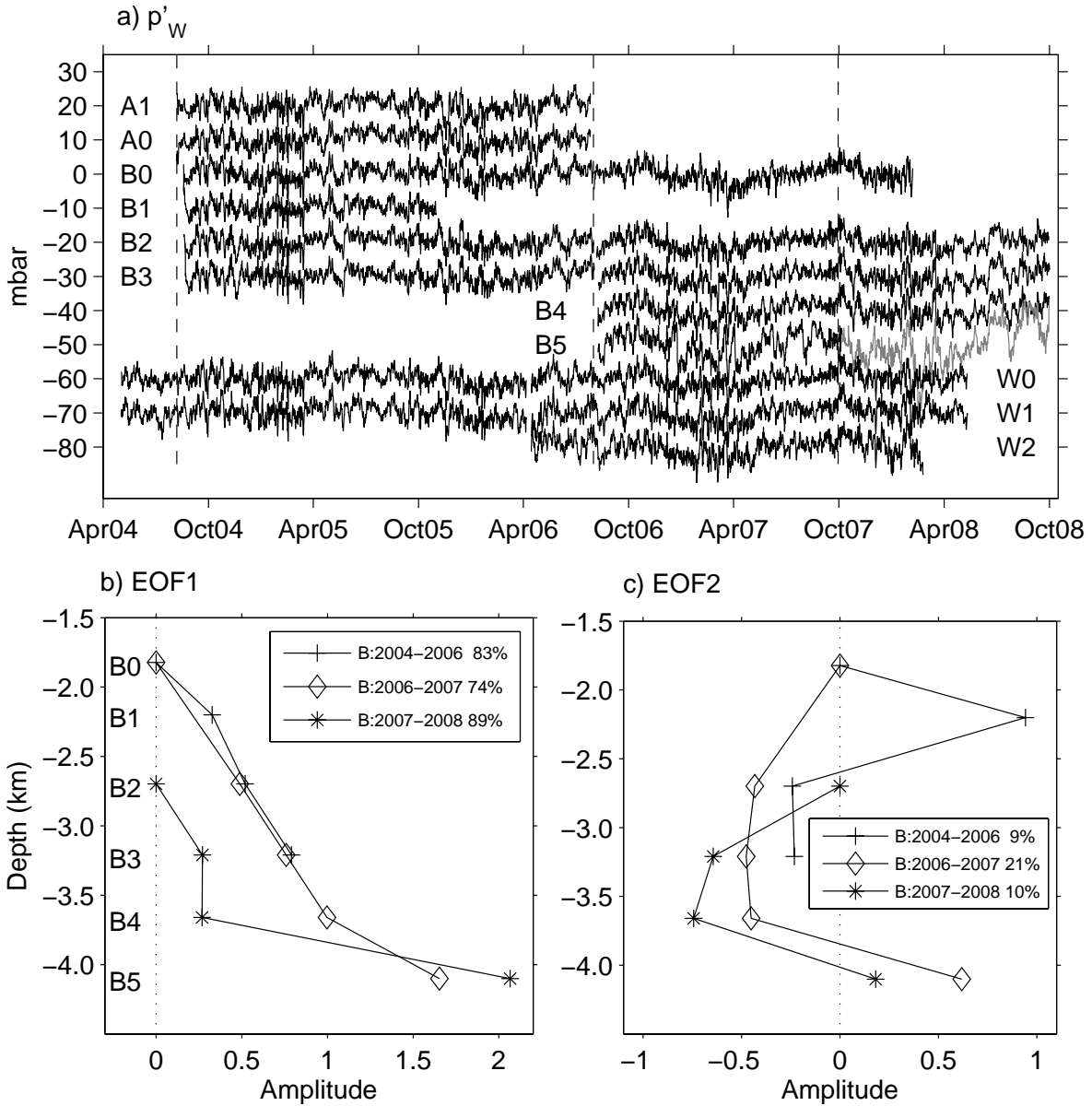


FIG. 4. a) Western boundary pressure anomalies at Line A moorings A0 and A1, Line W moorings W0 to W2, and Line B moorings B0 to B5. The second recovered deployment at B5 plotted in gray exhibits larger variability at low frequencies and was not used for this study. The time series are lowpass filtered to retain periods longer than one day for this plot. b) EOF1 and c) EOF2 of Line B boundary pressure records minus the shallowest records (with a zero EOF amplitude by construction) for the three deployment periods 2004–2006, 2006–2007 and 2007–2008. The legend in each panel indicates the percentage of variance explained by the modes for each time period. For comparison purpose, the EOF1 amplitude in panel b) were scaled to align their slopes between the depths of B2 and B3.

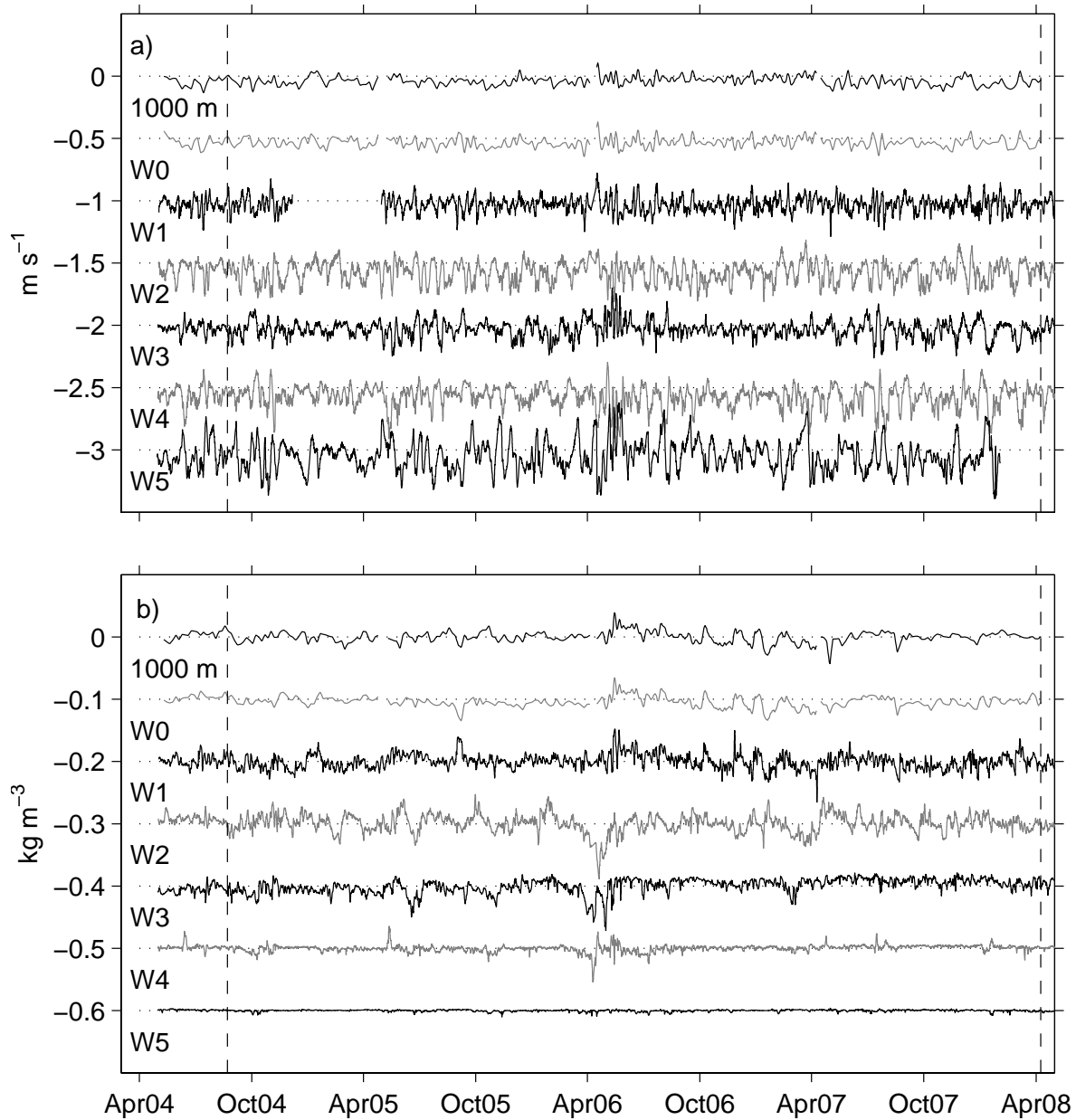


FIG. 5. Records at WHOI Line W of a) along slope velocity and b) in-situ density anomalies at 1000 m and the depth of W0 (1788 m) from the McLane profiler at W1, and from near-bottom current meters at moorings W1 to W5. For plotting purposes the time series at W1 to W5 were lowpass filtered to retain periods longer than 1 day.

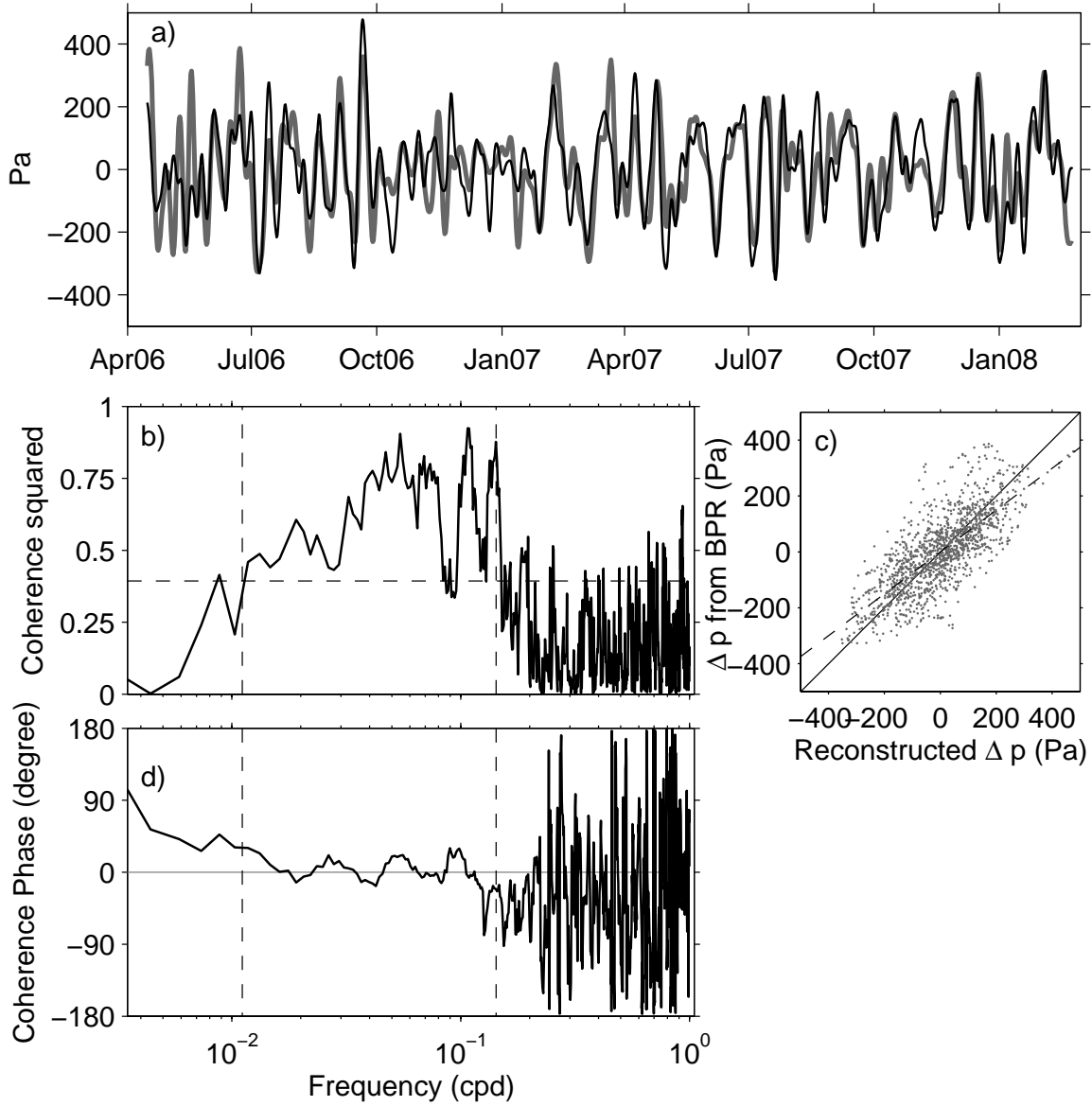


FIG. 6. Analysis of bottom pressure difference Δp between moorings W2 and W1; (a) from BPR data (black line) and reconstruction from density and velocity (gray line). Both time series are bandpass filtered to retain frequencies between $1/90$ and $1/7$ cpd indicated by vertical dashed lines in (b) and (d). (b) Coherence squared and (d) Coherence phase between the BPRs pressure difference and the reconstructed pressure difference. In (b), the horizontal dashed line indicates the 95% confidence level for coherence squared (the significant level is valid at any fixed frequency). (c) Scatter plots of the filtered reconstructed pressure differences (y -axis) and pressure differences from BPR data (x -axis) at 12-hour intervals. In this last plot, the dashed lines are the least squares fits to the scatter points (slope 0.74). For comparison, the solid black lines is the slope 1, intercept 0 curve.

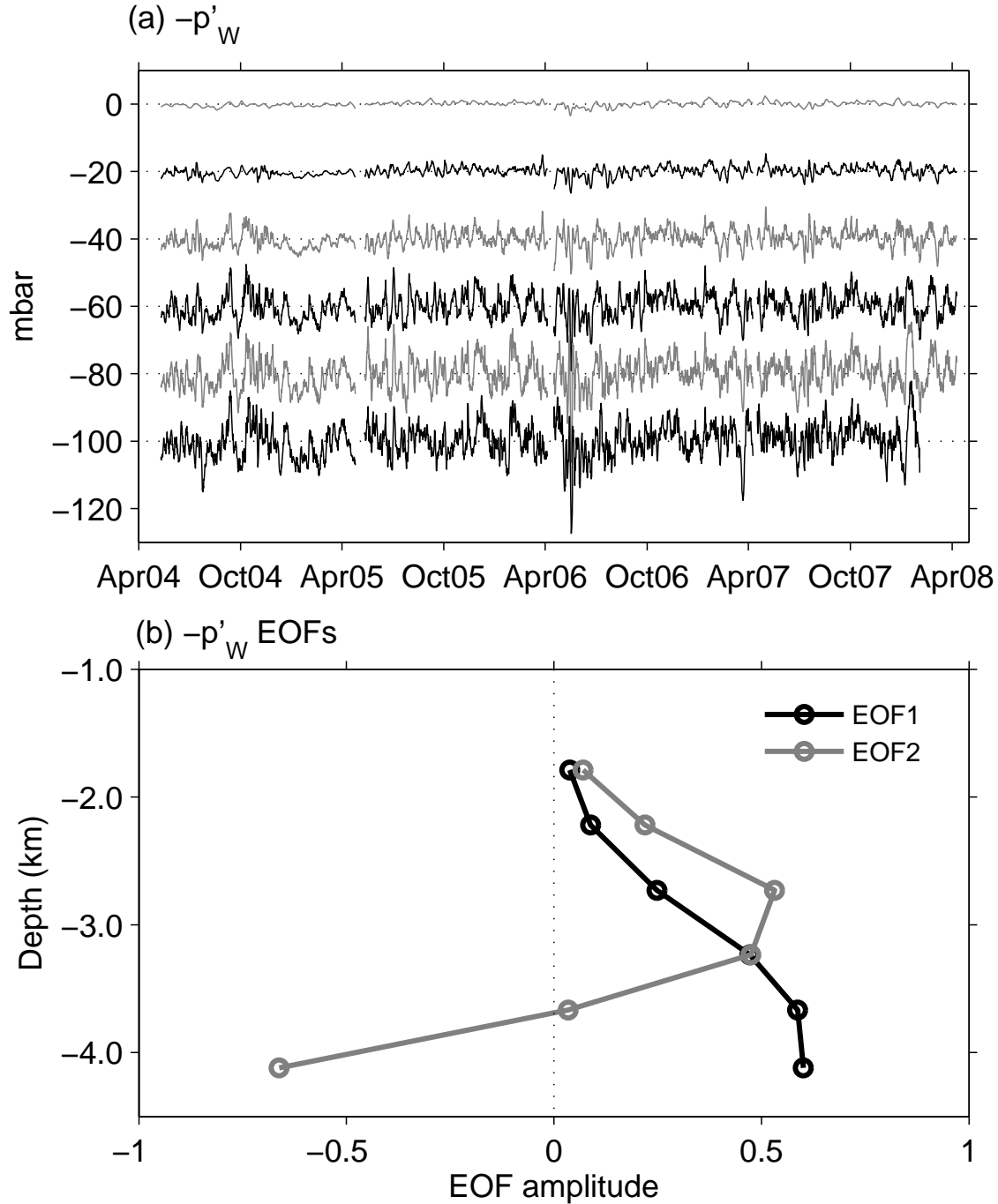


FIG. 7. Western boundary bottom pressure analysis at Line W. (a) Time series of western pressure anomalies $-p'_W$ at the depths corresponding to the base of mooring W0 (top curve) to W5 (bottom curve), subsequently offset by 20 mbar. Black and gray colors are alternated for legibility. One mbar is equivalent to a zonally-integrated northward volume transport of 1.08 Sv per km of depth, at this latitude. (b) First two EOF patterns of the pressure anomaly time series in (a) presented as a function of depth. The first mode explains 81.3% of the variance and the second mode 11.3%.

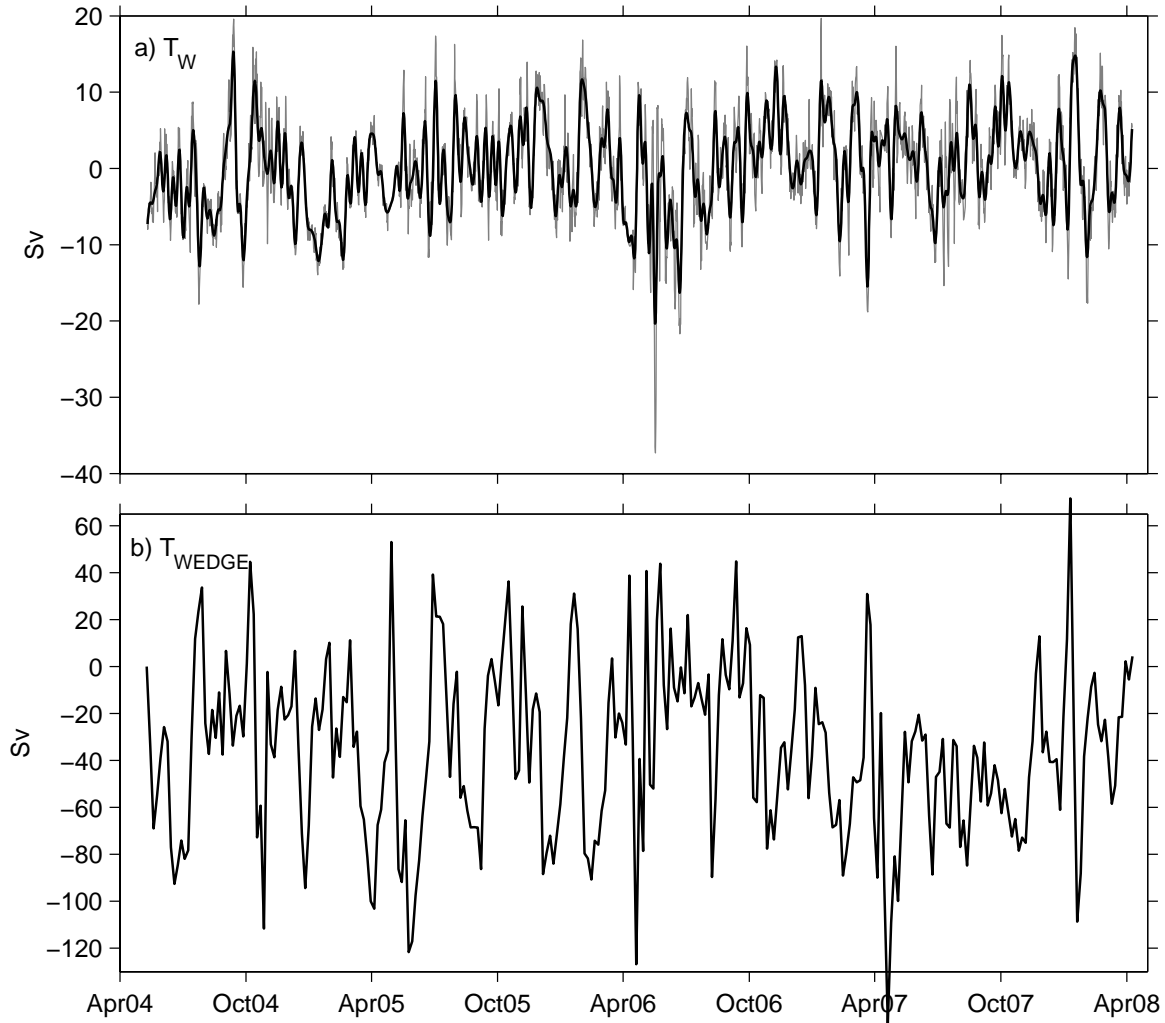


FIG. 8. (a) T_W : western overturning transport time series between 1000 m and 4120 m, relative to 1000 m. The gray line is the 12-h step time series and the black line is the 10-day lowpassed version. (b) T_{WEDGE} volume transport at Line W below 1000 m between the continental slope to the west and mooring W5 to the east (see Fig. 3). Note the different scales between a) and b).

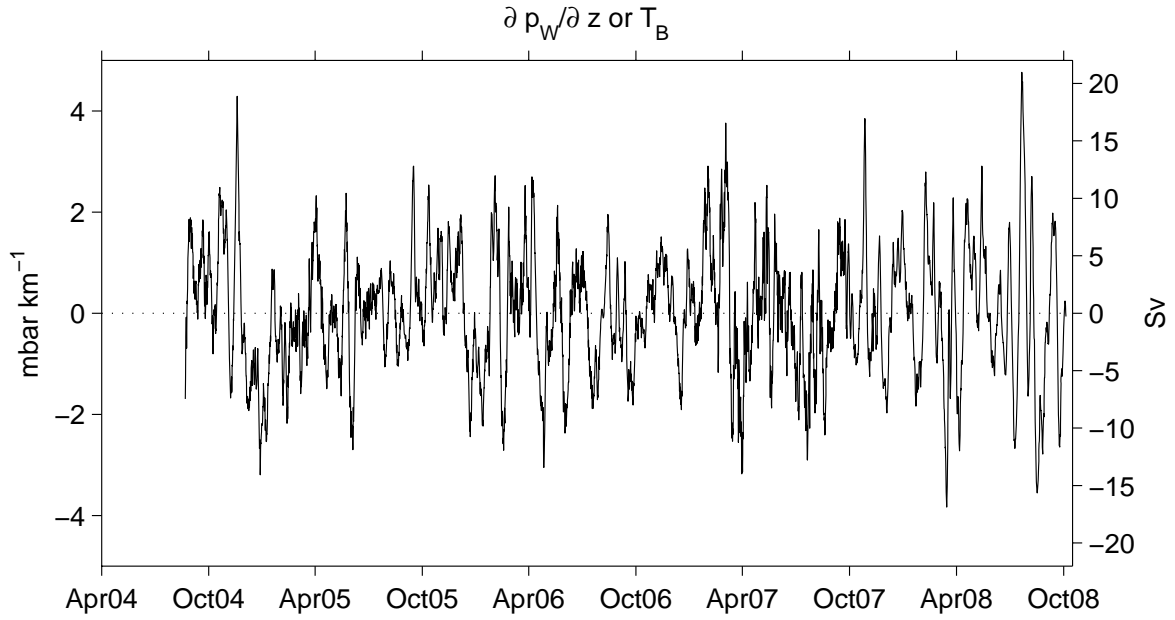


FIG. 9. Time series of western pressure gradient $\partial p_W / \partial z$ at Line B in mbar km^{-1} (left axis); the right axis is labeled in equivalent transport unit in Sv since the pressure gradient is integrated to obtain the layer transport T_B in the 1000 m to 4000 m depth range as $(\Delta z)^2 \partial p_W / \partial z / (2f \rho_0)$ with $\Delta z = 3000$ m, $f = 9.826 \times 10^{-5} \text{ s}^{-1}$, $\rho_0 = 1040 \text{ kg m}^{-3}$ (see text).

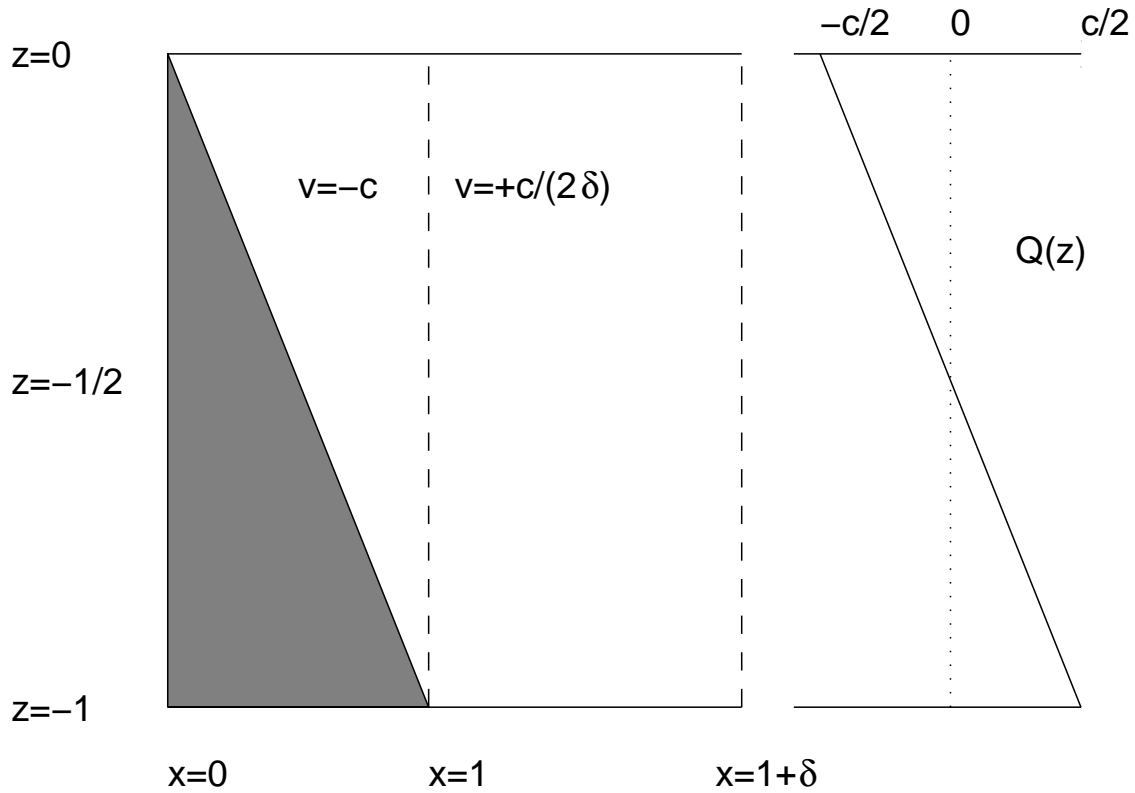


FIG. 10. Left: schematic of an idealized configuration of barotropic overturning. A current with uniform meridional velocity $v = -c$ flows over a continental slope (gray shading) which occupies the west part of the domain from $x = 0$ to $x = 1$ and between $z = 0$ and $z = -1$. A barotropic current with velocity $v = +c/(2\delta)$ of opposite sign flows over a flat bottom in the east part of the domain from $x = 1$ to $x = 1 + \delta$. Right: depth profile of the corresponding volume transport per unit depth $Q(z)$.

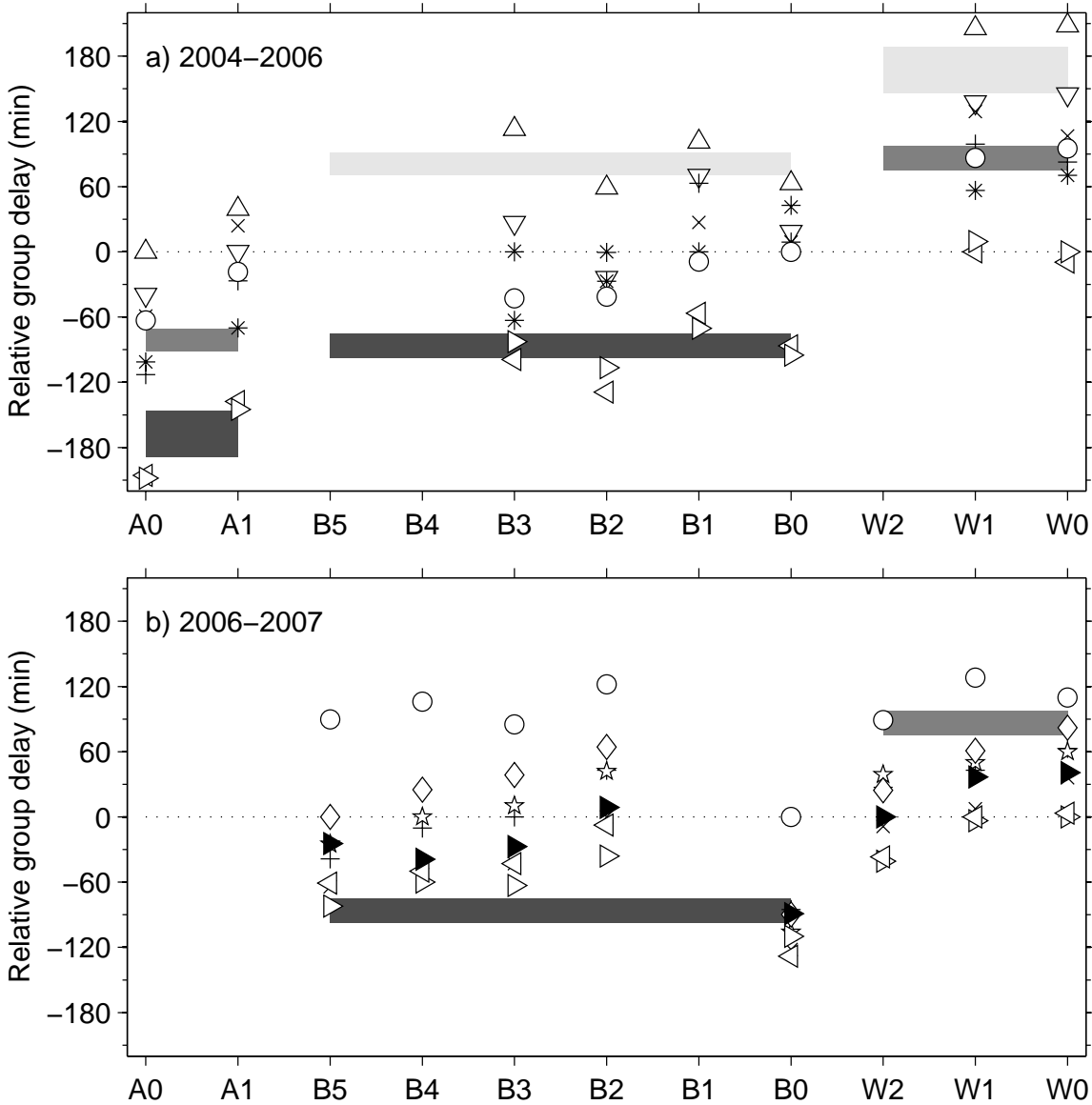


FIG. 11. Relative delay estimates between BPR record pairs for the time period May 2004 to April 2006 in a) and for August 2006 to October 2007 in b). Because these are relative delays for all pairs, values are plotted twice with opposite signs. The same symbols are used in both panels when appropriate to denote the delays estimated with respect to A0 (up pointing triangles), A1 (down pointing triangles), B0 (circles), B1 (asterisks), B2 (crosses), B3 (pluses), B4 (stars), B5 (diamonds), W0 (right pointing triangles), W1 (left pointing triangles), and W2 (black triangles). The boxes shaded light gray indicate a relative delay from Line A to lines B and W corresponding to a $170\text{--}220\text{ m s}^{-1}$ expected range of speeds. The boxes shaded medium gray indicate relative delays from Line B to lines A and W for the same speeds, and the boxes shaded dark gray from Line W to lines B and A. As an example in the top panel, it is estimated that a signal propagates from A0 to A1 in 40 min, from A0 to B0 in 63 min, from A0 to B1 in 101 min etc.

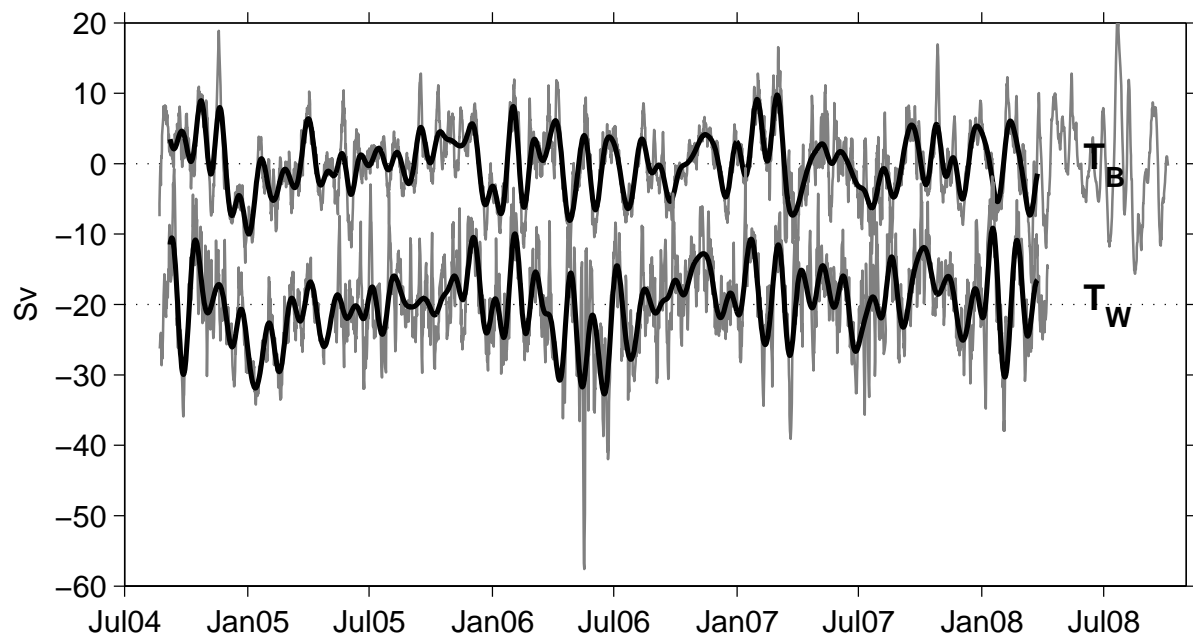


FIG. 12. T_B and T_W time series at 12-h intervals (gray lines). Both time series are anomalies with zero mean but T_W is offset by -20 Sv for legibility. The thick black curves are the 30-day lowpassed versions.

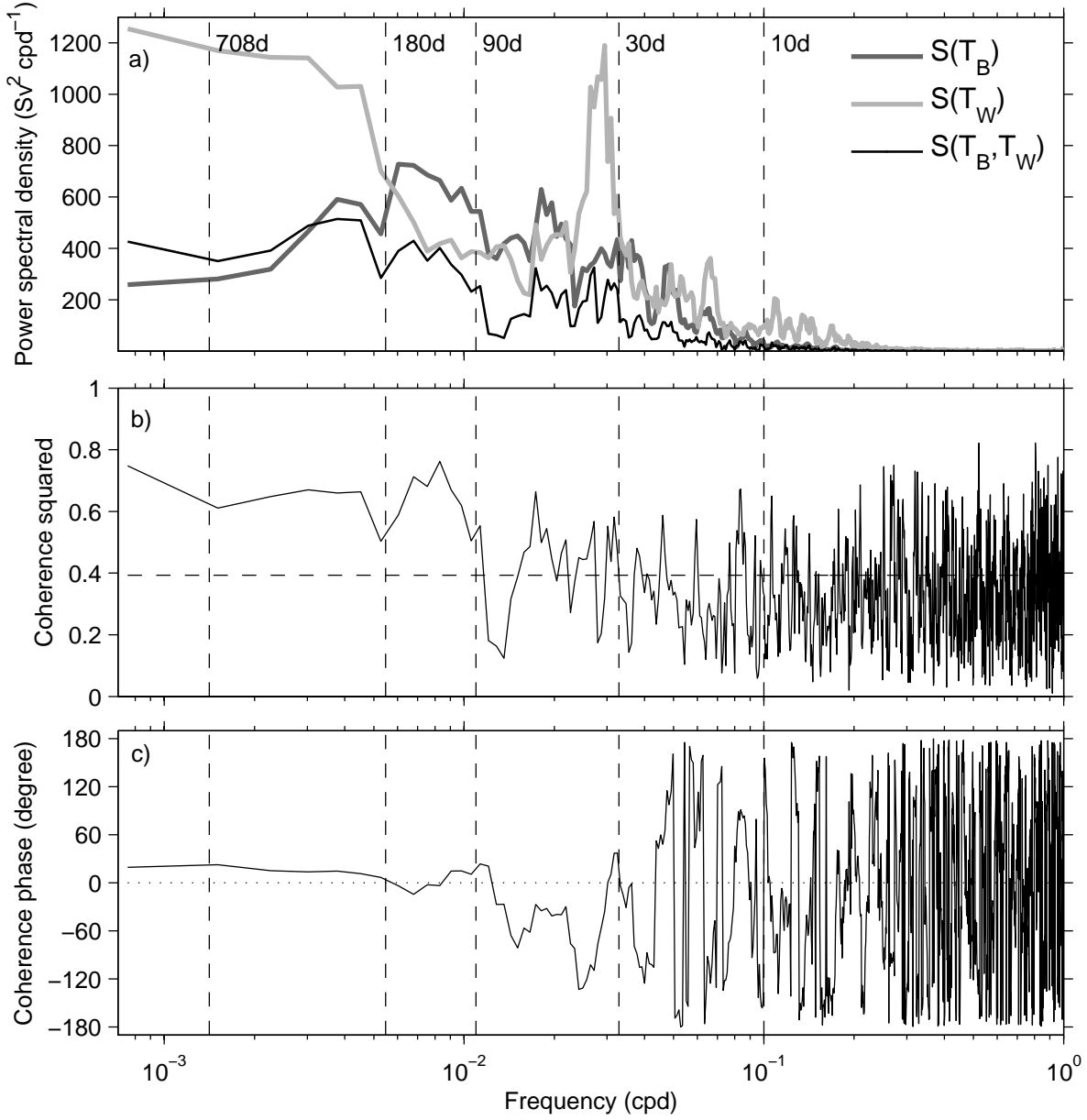


FIG. 13. Spectral analysis between T_B and T_W using a 7 Slepian tapers spectral estimate (Percival and Walden 1993). a) Auto spectral power density functions for T_B and T_W , and cross spectral density function between the two. The upper and lower limits of the formal 95% confidence intervals for the spectral density estimates based on the χ^2 probability distribution function with 7×2 degrees of freedom imply on this linear scale to multiply the curves by 0.5 and 2.5 approximately for each frequency value (these are not drawn for the legibility of the plot). b) Coherence squared. c) Coherence phase. The vertical dashed lines in all panels indicates the frequency limits which define the ranges in which the time delay estimations are conducted. A negative slope of the phase with frequency in c) indicates a possible propagation of a signal from Line B to Line W.

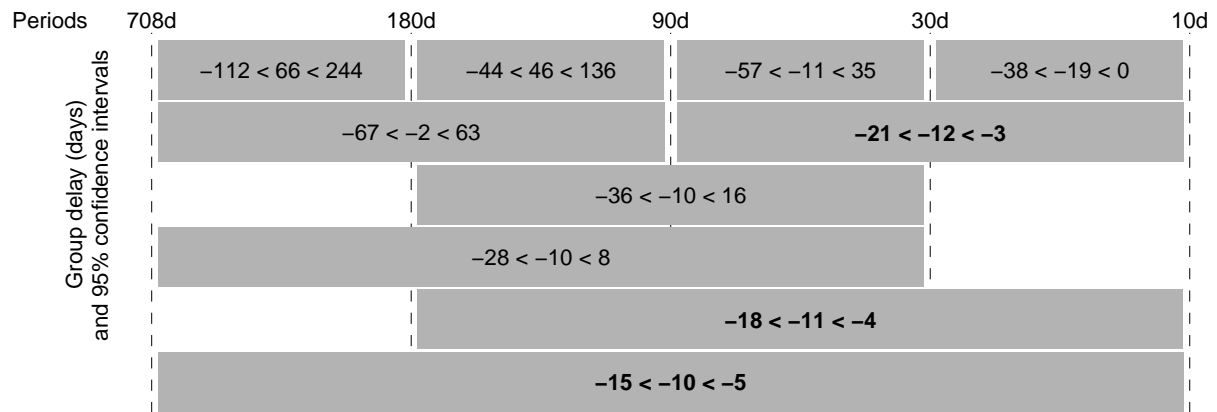


FIG. 14. Schematic of group delay estimates. These estimates are obtained for ranges of frequencies corresponding to the periods indicated at the top, also indicated in Fig. 13. Confidence intervals are at the 95% level. Group delay estimates which are different from zero according to the confidence intervals are in bold.

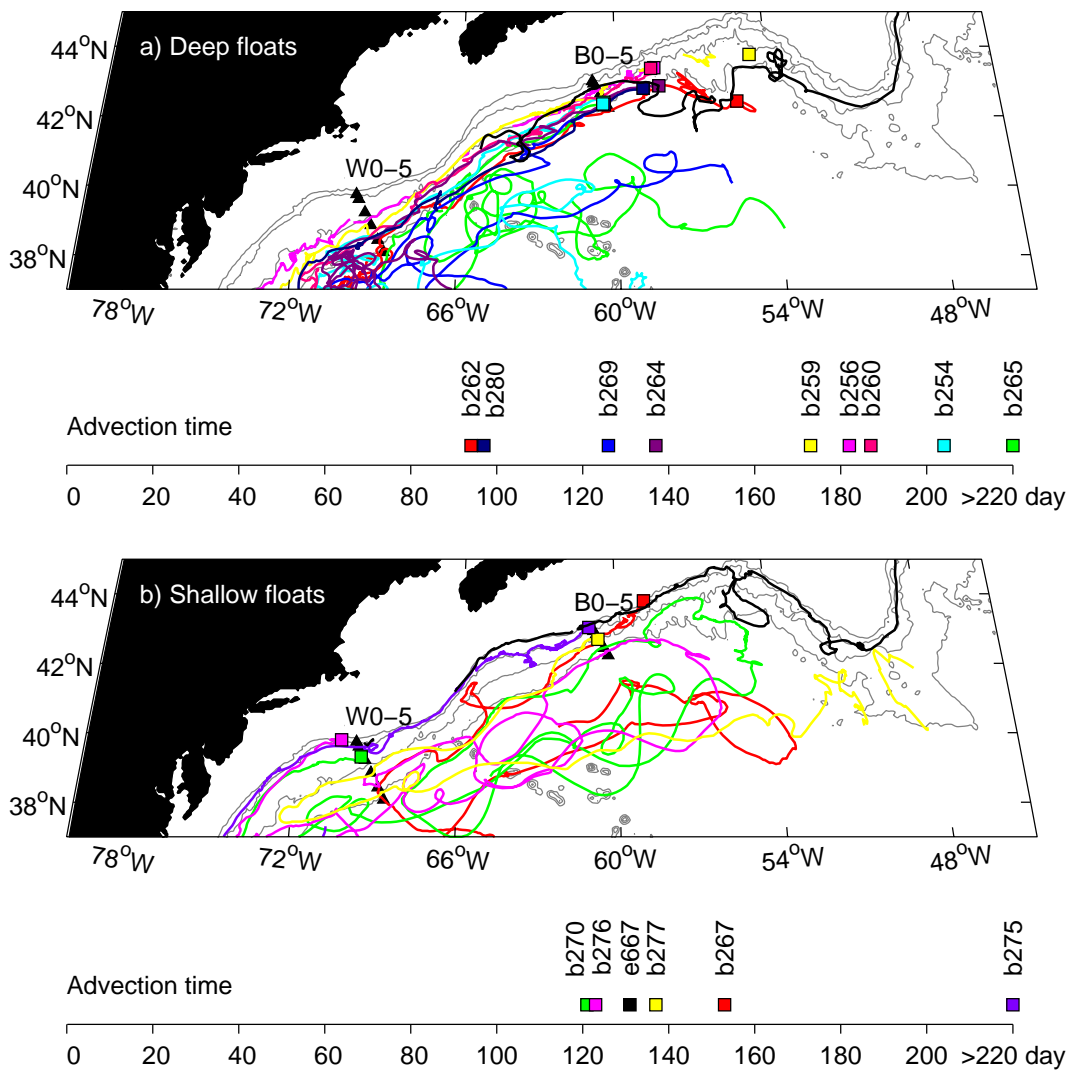


FIG. 15. a) Trajectories of deep RAFOS floats from the BOUNCE experiment which crossed perpendicularly both Line B and Line W (colored trajectories and square symbols at the launching locations) and one deep float from the ExPath experiment (black trajectory). The launching position of the ExPath float is outside of the map. The 1, 2, 3 and 4 km isobaths are contoured in gray. The locations of Line B and Line W moorings are indicated by black triangles. The corresponding advection times in days are reported on the horizontal scale below the map. b) Same than a) but for shallow floats of BOUNCE and one shallow float from ExPath which flowed in this region (black trajectory) but which launching position is outside of this region.

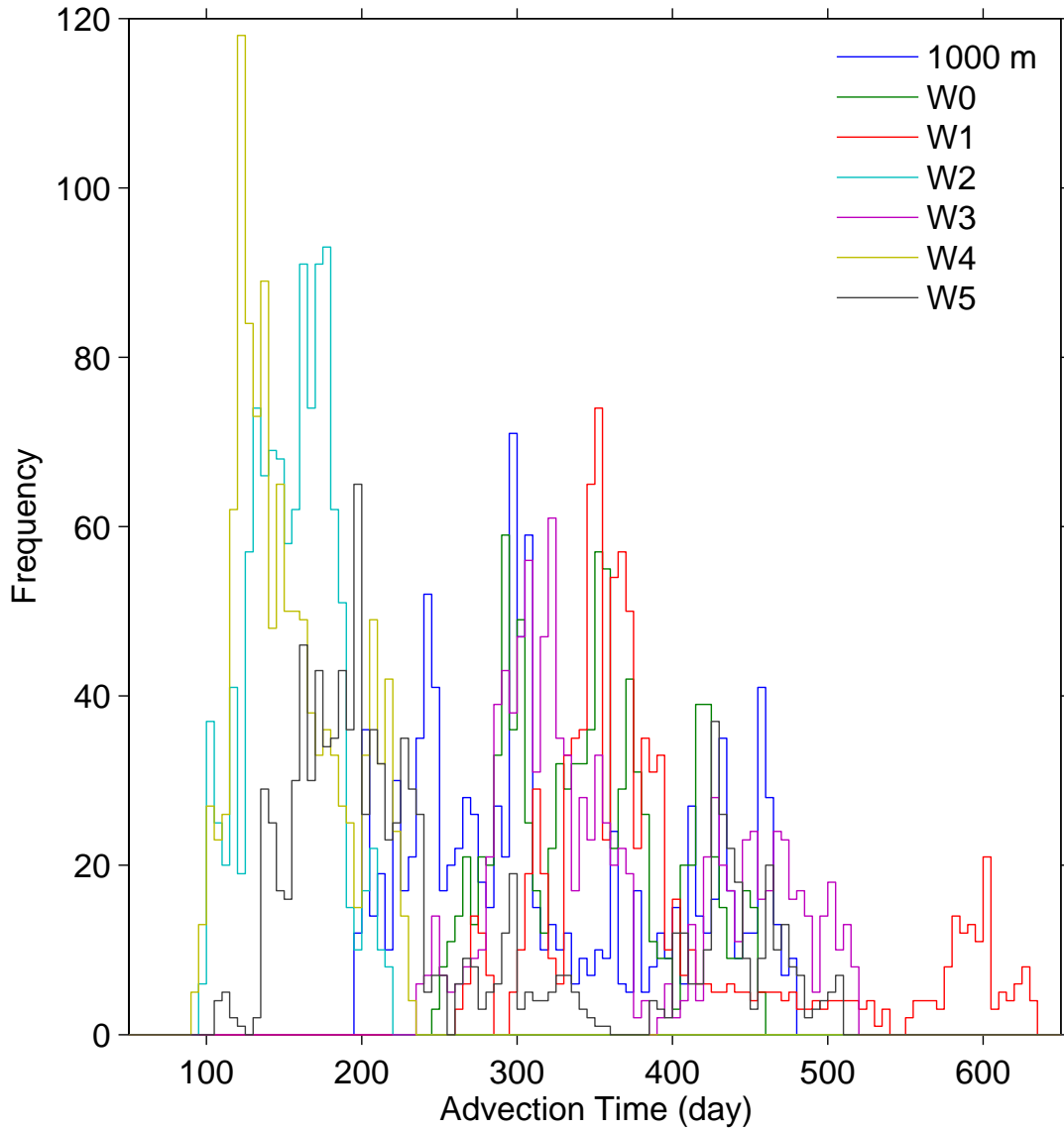


FIG. 16. Distribution of advection time scales between Line W and Line B based on integrating the velocity time series shown in 5a).